



# Stratification effects on hydrodynamics and mixing at a river confluence with discordant bed

Zhengyang Cheng<sup>1,2</sup> · George Constantinescu<sup>1</sup>

Received: 7 August 2019 / Accepted: 26 November 2019 / Published online: 6 December 2019  
© Springer Nature B.V. 2019

## Abstract

Stratification effects induced by density differences between the incoming flows are investigated at a medium-size stream confluence with a highly discordant bed. The relatively large temperature difference  $\Delta T = 4.7$  °C between the main, high-discharge tributary and the low-discharge tributary together with the relatively small velocity of the flow in the main channel translate in a very high Richardson number,  $Ri = 1.89$ , which suggests that stratification effects have an important effect on flow hydrodynamics and thermal mixing. Simulation results confirm this and show that for the case when the velocity of the low-discharge, lower-temperature tributary is much smaller than that of the high-discharge tributary, the denser fluid from the low-discharge tributary plunges rapidly toward the bottom and the confluence apex. It then moves as a near-bed current of denser fluid across the main-tributary side of the main channel until the opposing bank where it reaches the free surface. It then continues to move parallel to the bank line. Meanwhile, the less-dense fluid from the main tributary moves over the near-bed current of denser fluid into the central part of the main channel. This induces a two-layer structure of the flow inside the upstream part of the confluence, which explains the very different mean flow patterns near the bed and near the free surface. Flow hydrodynamics and mixing in the  $Ri = 1.89$  simulation are found to be very different when compared to those observed in the no-density-effects ( $Ri = 0$ ) case where there is no coupling between the temperature and the momentum equations via the Boussinesq approximation. In this case, the fluid from the low-discharge tributary remains on the corresponding side of the main channel. Away from the confluence apex, the volume of mixed fluid is several times larger in the  $Ri = 1.89$  simulation, which demonstrates that under certain conditions two streams of unequal densities can mix much faster compared to the case when the two streams have the same density. The large-scale flow patterns, eddy dynamics and volume of mixed fluid in the  $Ri = 1.89$  simulation were also found to present major differences with a case where the main, high-discharge tributary contained the lower-temperature (denser) fluid.

**Keywords** River confluences · Vortices · Mixing layers · Turbulent mixing · Stratification effects

---

✉ George Constantinescu  
sconstan@engineering.uiowa.edu

Extended author information available on the last page of the article

## 1 Introduction

Besides planform geometry and momentum/velocity ratio of the incoming flows, flow hydrodynamics, mixing and transport of matter and sediments at river confluences are a strong function of the degree of bed discordance [1, 20, 21, 27, 28, 34, 40, 42–45, 48]. When a small tributary merges with a large stream, a large bed discordance is generally present around the confluence apex. In some cases, the flow in the shallower tributary separates as it enters the confluence [19]. The degree of three-dimensionality of the flow field increases significantly starting near the confluence apex [8, 11, 19, 20, 42, 45, 46] and hydrodynamics zones with different properties are observed downstream of the confluence apex [5]. For example, Boyer et al. [6] observed strong upwelling motions from the deeper tributary side toward the shallower tributary side inside the confluence hydrodynamic zone. Leite-Ribeiro et al. [27–29] observed that while the near-bed flow from the deeper tributary continues to advance with minimum change in direction inside the main channel, the flow near the free surface is deflected by its interaction with the flow from the shallower tributary.

As the two streams come into contact, a region where the streamwise velocity, turbulence intensity and the values of the transported scalar (e.g., temperature in the case of incoming streams with unequal temperatures) vary rapidly in the cross-stream direction forms [24]. This region is called the mixing interface (MI) region [16]. In the case of a small bed discordance, the MI contains counter-rotating (Kelvin–Helmholtz mode is dominant for momentum and velocity ratios much larger or much smaller than one) or co-rotating (the wake mode is dominant for momentum and velocity ratios close to one) vertically-oriented vortices [13, 15, 16]. For a sufficiently large bed discordance, the structure of the MI can be quite different, as the vertically-oriented vortices forming close to the confluence apex may not be present in the downstream part of the confluence hydrodynamic zone. An important type of coherent structures observed to form at concordant confluences with a high angle between the tributaries are streamwise-oriented vortical (SOV) cells [13, 16, 19, 34]. These cells form beneath the free surface on one or both sides of the MI in the region where the two streams collapse. As bed discordance increases, SOV cells are either suppressed or their coherence is greatly diminished [11, 19, 27, 28]. This is very relevant given the fact that SOV cells were found to be a main mechanism for entrainment and transport of sediments inside the confluence hydrodynamic zone, to redistribute the streamwise momentum and to enhance mixing between the two streams [15–18, 49]. Thus, mixing mechanisms, sediment transport and morphodynamics can be very different at confluences with a large bed discordance compared to concordant confluences [6, 20, 21, 27, 28].

Further complicating the flow hydrodynamics is the effect of density differences between the incoming flows, which can induce strong stratification effects downstream of the confluence apex, near which an initially vertical density interface is present if the temperature, salinity and/or suspended sediment load of the incoming flows are different [7, 11, 13, 26, 30–32, 35–37]. Such conditions are common in natural river confluences, especially for those where a colder tributary containing water from the mountains merges with the main stream [39]. Recent studies have shown that mixing mechanisms are quite different in the presence of relatively large density difference between the incoming flows (e.g., densimetric Froude numbers defined with the mean main channel velocity and the relative density difference between the two streams less than 10), which results in the two streams mixing at a very different rate compared to the case when the density difference is negligible [11, 30]. However, there is no clear understanding on how stratification affects mixing.

In fact, in some cases mixing was found to enhance with increasing density contrast while in others the effect of density contrast on mixing was small or acted toward inhibiting mixing [11, 13].

Downstream of the confluence apex, the initially vertical density interface between the two streams is unstable because of differences in the hydrostatic pressure on its sides, away from the free surface. The flow tries to become stably stratified. Its evolution toward this state (e.g., over what distance from the apex the flow becomes stably stratified) is a function of the momentum/velocity ratio, planform geometry and degree of bed discordance. In the case of concordant confluences, the evolution toward a stably stratified state happens via the development of a lock-exchange-like flow in spanwise cross-sections, as denser fluid moves into the less-dense-fluid side near the bed, while the opposite happens near the free surface [13]. The interface between the fluids becomes close to horizontal (stable stratification) when the fronts of the currents containing denser and less-dense fluid from the two incoming flows reach the banks of the main channel. The development of the lock-exchange flow can also affect the coherence of the SOV cells and their positions, if such cells form in the vicinity of the MI. How fast the flow inside the confluence becomes stably stratified is controlled by the Richardson number ( $Ri = g'D/U_0^2$ , where the reduced gravity is  $g' = (\Delta\rho/\rho_0)g$ ,  $\rho_0$  is the average density of the two streams and  $g$  is the gravitational acceleration) or, equivalently, the densimetric Froude number ( $Fr_p = 1/Ri^{1/2}$ ). Both numbers are defined with the mean velocity inside the main channel,  $U_0$ , the mean flow depth inside the main channel,  $D$ , and the density difference of the incoming flows,  $\Delta\rho$ . Moreover, there is evidence that density contrast between the incoming flows can generate large-scale coherent structures inside the confluence, while dampening or suppressing others (e.g., the vertical Kelvin–Helmholtz billows generated inside the MI) with respect to the case the densities of the incoming flows are equal. This is the case for both concordant and discordant confluences [11, 13]. Consequently, stratification can enhance some mixing mechanisms (e.g., via the spatially-developing lock-exchange flow), while suppressing others, especially at large distances from the confluence apex.

Large-eddy simulation based techniques were successfully used to investigate hydrodynamics and transport processes at river confluences (e.g., see [13, 47]. Similar to Cheng and Constantinescu [11], Detached Eddy Simulations (DES) are performed to investigate flow, turbulence and mixing mechanisms at the strongly-discordant-bed confluence of the Ebro River and Segre River in Spain, for which detailed descriptions of the bathymetry and flow conditions are available from field studies (e.g., [1, 36]. Stratification effects are simulated using the Boussinesq form of the Navier–Stokes equations and solving an additional transport equation for the nondimensional density/temperature.

In the present study, we investigate how density contrast induced by mean temperature differences between the incoming flows affects hydrodynamics (e.g., eddies generated inside the MI, flow structure near the confluence apex, recirculation regions and associated large-scale unsteadiness, dynamics of the eddies generated by separated shear layers) and mixing processes for a case where the shallower tributary contains the denser, lower temperature fluid (see flow conditions on October 11, 2011 in Table 1). A second simulation is performed for a no-density-effects case. In this latter simulation, the effect of the temperature differences on the density field is neglected. In the simulations discussed in the present paper, the temperature of the deeper, high-discharge tributary is larger than that of the shallower tributary, while the opposite was true for the simulations reported by Cheng and Constantinescu [11]. As the physical Richardson number is larger in the present stratified-flow case ( $Ri = 1.89$ ) compared to the case ( $Ri = 0.67$ ) investigated by Cheng and Constantinescu [11], one expects stratification effects will be stronger. Moreover, stratification is

**Table 1** Main parameters (volumetric discharge and mean temperature of the two tributaries, temperature difference, mean velocity in the main channel, velocity ratio, momentum ratio, Richardson number and densimetric Froude number) of the confluence flow simulations performed for field conditions

	$Q_{\text{EBRO}}$ ( $\text{m}^3/\text{s}$ )	$Q_{\text{SEGRE}}$ ( $\text{m}^3/\text{s}$ )	$T_{\text{EBRO}}$ ( $^{\circ}\text{C}$ )	$T_{\text{SEGRE}}$ ( $^{\circ}\text{C}$ )	$\Delta T$ ( $^{\circ}\text{C}$ )	$U_0$ ( $\text{m}/\text{s}$ )	VR	MR	Ri	$Fr_p$
March 31, 2011	493	91	10.7	15.0	-4.3	0.18	0.41	0.075	0.67	1.21
October 11, 2011	397	16	21.0	18.3	2.7	0.108	0.08	0.0032	1.89	0.73

expected to affect in a very different way flow hydrodynamics and mixing in the  $Ri = 1.89$  simulation reported here compared to the  $Ri = 0.67$  simulation, as the denser fluid will move laterally in opposite directions near the bed in these two simulations, once the two incoming flows come into contact.

Section 2 describes the test cases. Section 3 briefly introduces the numerical model and discusses the setup of the simulations and relevant validation cases. Section 4 discusses differences in the mean flow and mean temperature patterns with the limiting, no-density-difference case and with the case discussed in Cheng and Constantinescu [11] where the near bed intrusion of denser fluid develops in the opposite direction. Section 5 extends this comparison to the dynamics of the eddies generated inside the MI and the large-scale unsteadiness associated with the recirculation region forming near the confluence apex. These flow hydrodynamics features are found to generate important mixing mechanisms, as explained in Sect. 6. Section 7 shows that the regions of large amplification of the turbulence are induced by the large-scale eddies generated in the flow, in particular those forming inside the MI and the shear layers between regions with different mean streamwise velocities. Section 8 analyzes the effect of density contrast on the mean bed shear stress and its root mean square values. Based on this information, the capacity of the flow to entrain sediment, or to induce sediment deposition, is discussed. Section 9 summarizes the main results and focuses on the differences in flow hydrodynamics and mixing between the case where the high-discharge tributary contains the denser fluid and the case the same tributary contains the less dense fluid. It also relates the present findings with observations at other natural river confluences with significant density contrast between the incoming streams.

## 2 Test cases

The main characteristics of the confluence of the Ebro River and the Segre River have been presented in Cheng and Constantinescu [11]. The two tributaries merge at an angle close to  $110^{\circ}$  (Fig. 1). The deepest parts of the Ebro River channel are about  $1.6D$  deeper than the deepest parts of the Segre River channel, where  $D \approx 4$  m is the average flow depth in the main channel. The ratio between the flow depths in the two incoming channels in the present simulations is 2.2, which is very close to values (1.8–2.2) observed at other confluences with a strong bed discordance [6, 19, 21, 22]. Despite being shallower, the Segre River is much wider. In both tributaries, the flow depth is very non-uniform in the transverse direction. Downstream of the confluence, the main channel is much deeper near the South Bank. A sharp increase in the bed elevation occurs at about  $1/3 W$  from the South Bank (Fig. 2), where  $W \approx 110D$  is the mean width of the downstream channel.

**Fig. 1** Planform geometry and bathymetry at the confluence of the Ebro River and the Segre River. The contours corresponds to lines of constant vertical elevation,  $z/D$ , where the free surface is situated at  $z/D=0$  and  $z$  is positive upwards. Also shown are the cross-sections where the solution is analyzed

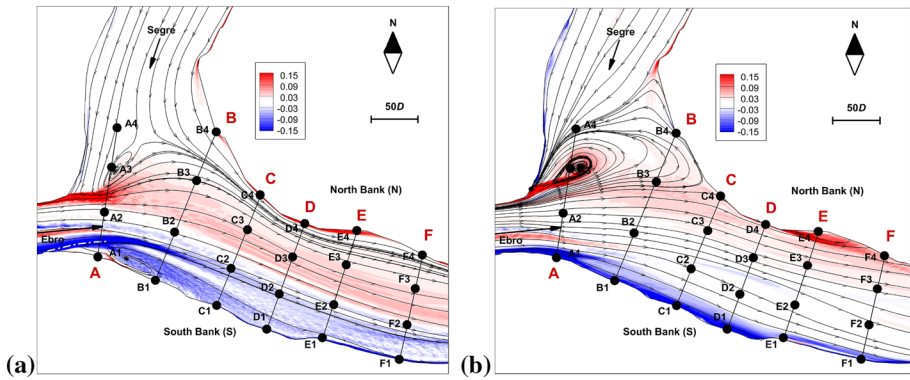
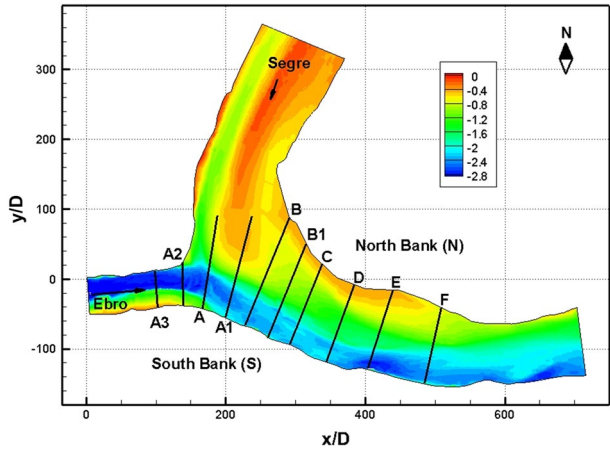


**Fig. 2** Distribution of vertical vorticity,  $\omega_z D/U_0$ , and 2-D streamline patterns in a plane situated near the free surface ( $z/H = -0.1$ ) in the mean flow. **a**  $Ri = 0$ ; **b**  $Ri = 1.89$

The conditions in the case with non-equal densities of the incoming streams discussed in this paper correspond to the flow conditions recorded on October 11, 2011 (see Table 1). Close to the confluence apex, the mean velocities in the incoming channels were 0.2 m/s and 0.016 m/s, respectively. The mean velocity in the main channel was  $U_0 = 0.108$  m/s. The velocity ratio of the incoming tributary flows is  $VR = 0.08$ , while the momentum ratio is  $MR = 0.0032$ . The temperature difference between the incoming streams was  $\Delta T = T_{EBRO} - T_{SEGRE} = 2.7$  °C, which corresponds to  $Ri = 1.89$ . The inflow section temperatures were measured at several points along the transects using a Seabird SBR-19 conductivity-temperature-depth CTD profiler. The confluence bathymetry was obtained using an Acoustic Doppler Current Profiler. More details on the field experiments are given in Ramón et al. [36]. Table 1 also lists the flow conditions on March 31, 2011 corresponding to the simulation discussed by Cheng and Constantinescu [11]. The contribution of the suspended sediment concentration to the relative density difference between the two streams is fairly negligible compared to that due to temperature differences (see also discussion in [36]). The model does not include heat exchange at the free surface nor wind shear effects. The densimetric Froude numbers in the  $Fr_p = 0.73$  and 1.21 simulations are slightly larger

than those ( $0.13 < Fr_p < 0.7$ ) considered in the RANS-based numerical study of Ramón et al. [37].

A second (no-density-effects) simulation was conducted with the flow conditions present on October 11, 2011. The Boussinesq term in the vertical momentum equation of the numerical model was set to zero, which corresponds to a case with  $Ri = 0$  or  $Fr_p = \infty$ .

There are two main differences between the density effects ( $Fr_p = 0.73$ ,  $Ri = 1.89$ ) case investigated in this study and the one ( $Fr_p = 1.21$ ,  $Ri = 0.67$ ) investigated by Cheng and Constantinescu [11]. The first one is that the present investigation considers a case in which the low-momentum and low-velocity tributary contains the denser fluid, while the opposite was true for the case discussed by Cheng and Constantinescu [11]. As a result, the intrusions will develop in opposite directions close to the free surface and the bed in the two cases, which induces large differences in the flow structure and affects how the two streams mix. The second difference is that the discharge ratio, the velocity ratio and the momentum ratio are close to 6, 5 and 22 times, respectively, smaller in the  $Ri = 1.89$  case. This means that the case investigated here is close to the limiting case when a fast stream comes into contact with a reservoir containing denser fluid, a case that is fairly common at both concordant and discordant bed confluences. For such flow conditions, the mixing mechanisms and their relationship to the large-scale flow structure and turbulent eddies generated in the flow were not yet investigated in the literature. Moreover, comparison with the limiting no-density-difference case, allows isolating the effects associated with flow stratification for a case where the velocity and discharge of the secondary tributary are more than one order of magnitude smaller than those of the main tributary. To make it easier to understand the differences in flow hydrodynamics and mixing mechanisms at discordant bed confluences between cases where the denser fluid is situated in the secondary (low-discharge) tributary and cases where the denser fluid is situated in the main (high-discharge) tributary, the discussion of results follows the same structure and presents similar information to the one included in Cheng and Constantinescu [11]. Given that both the velocity ratio and the momentum ratio are lower in the present simulations compared to those reported in Cheng and Constantinescu [11], either VR or MR can be used to characterize the differences in the properties of the incoming flows. To be consistent with the companion paper, we refer to each case by mentioning the VR and Ri values.

### 3 Numerical model, boundary conditions and code validation

As opposed to large eddy simulation (LES) models employing wall functions, DES uses a more sophisticated RANS-based model close to solid boundaries and then transitions toward a particular form of the LES closure away from these boundaries [41]. This allows capturing the dynamics of the energetically important eddies in the flow with a reasonable amount of computer resources at relatively large Reynolds numbers (e.g., field scale conditions for rivers). The numerical algorithm and DES model are the same as the ones used by Cheng and Constantinescu [11]. Detailed descriptions of the fractional-step algorithm used to solve the discretized Navier–Stokes equations, the method used to solve the discretized advection–diffusion equation for the nondimensional temperature/concentration, the discretization of the different terms, code, the one-equation, Spalart–Allmaras DES model and the implementation of rough-wall boundary conditions are given in Constantinescu et al. [14, 15], Chang et al. [9], Zeng et al. [50], Rodi et al. [41] and Cheng and Constantinescu [11].

The nondimensional vertical momentum equation contains the Boussinesq term,  $-C' \cdot Ri$ , where  $C' = (T_{\text{EBRO}} - T) / (T_{\text{EBRO}} - T_{\text{SEGRE}})$  is the nondimensional temperature,  $T(x, y, z, t)$  is the dimensional temperature field. For cases with  $Ri > 0$ ,  $C'$  also corresponds to the nondimensional density field. The molecular Prandtl number was assumed to be equal to six in the transport equation for  $C'$ , which is within the normal range of values used for temperature transport in water bodies. The turbulent Prandtl number in the  $VR = 0.08$ ,  $Ri = 1.89$  simulation ( $Pr = 1.4$ ) was specified using the procedure proposed by Zilitinkevich et al. [51] to account for buoyancy effects, while a unity value was assumed in the  $VR = 0.08$ ,  $Ri = 0$  simulation.

The free surface was modeled as a symmetry, no-shear boundary, a convective boundary condition was used at the outflow and the velocity fields at the inlets of the tributary channels were obtained from preliminary DES simulations of constant-temperature, fully-developed open channel flow. This means that the specified inflow boundaries neglect the presence of secondary flow. The tributary channels do not contain upstream regions of high channel curvature in the vicinity of the two inflow sections, so secondary flow is not expected to be very strong at these locations. The channel bottom and banks were modeled as no-slip, rough surfaces. The normal gradients  $C'$  were assumed to be equal to zero at all boundaries, except for the boundaries where the values  $C'$  are imposed. The constant values specified at the two inlet sections were  $C' = 1$  for the Segre River and  $C' = 0$  for the Ebro River. The fields of  $C'$  are also used to quantify mixing. Mixed fluid is defined as fluid with  $0.1 < C' < 0.9$ .

The computational mesh contained close to 22 million cells with about 30 points distributed along the vertical direction. About 350 points were distributed over the width of the main channel. The horizontal cell aspect ratio was close to one away from the solid boundaries. Away from the banks and the regions situated near the confluence apex, where Kelvin–Helmholtz billows are forming, the average cell size in the horizontal directions was close to  $0.3D - 0.7D$ . In the vertical direction, the cell size was close to  $0.05D$  close to the free surface. Grid points were clustered near the bank lines and the confluence apex to resolve the flow inside the attached boundary layers and the shear layers. The first point off the channel bed was situated at around 2 wall units away from the solid surface. The non-dimensional time is defined as  $t_0 = D/U_0$ . The time step was  $0.005t_0$ . The Courant number in the cells situated away from the solid surfaces was less than 0.1. Figure 1 shows the main cross sections at which the  $VR = 0.08$ ,  $Ri = 0$  and  $VR = 0.08$ ,  $Ri = 1.89$  simulations are compared.

The same DES solver was used to study flow hydrodynamics and mixing processes at field scale conditions for a small natural river confluence with concordant bed [15–18]. Laboratory scale investigations were conducted for a small mountain-river confluence with a large bed discordance [23] and for a shallow mixing layer developing at the confluence between parallel streams [10, 13] for cases where density difference effects on flow hydrodynamics were negligible. These studies contain extensive validation with field and lab data of the mean streamwise velocity, mean temperature and turbulent kinetic energy (TKE) predictions, position of the MI, passage frequency of the billows forming inside the MI, as well as on the formation and position of some of the main vortices in the flow. Cheng and Constantinescu [11] contains some qualitative validation of the free-surface mixing patterns between the Segre River and the Ebro River and of the position of the MI for a case with  $Ri \approx 0$ . Orr et al. [33] discuss validation of the same solver using the Boussinesq approximation for stratified flows.

## 4 Mean flow

The mean-flow vertical vorticity distribution in the  $VR=0.08$ ,  $Ri=0$  case shows that no separated shear layer (SSL) forms on the Segre River side of the confluence apex. Meanwhile, the vorticity amplification is large inside the SSL forming on the Ebro River side (Fig. 2a). Further downstream, this SSL develops into a thick region of high, same-sign vorticity, which suggests that the MI is in the Kelvin–Helmholtz (KH) mode, consistent with the value of the velocity and momentum ratios near the confluence apex ( $VR=0.08 \ll 1$ ,  $MR=0.0032 \ll 1$ ). The main difference with the no-density-effects ( $VR=0.41$ ,  $Ri=0$ ) case discussed by Cheng and Constantinescu [11] is the absence of a wake region near the confluence apex, which is expected given that no SSL forms on the Segre River side for  $VR=0.08$ . At around  $20D$  from the confluence apex, the vorticity levels inside the SSL decay sharply and the width of the region characterized by vorticity levels larger than those in the surrounding turbulent flow ( $\omega_z D/U_0 > 0.1$ ) increases suddenly to about  $35D$ . This region extends until the end of the computational domain, is situated on the Segre River side of the main channel but does not touch the North Bank. A similar high vorticity region was observed in the  $VR=0.41$ ,  $Ri=0$  simulation, but its average width was only  $25D$ . Due to the high curvature of the South Bank around section A, a strong SSL forms as the core of high velocities from the Ebro River enters the confluence hydrodynamic zone. Large-scale energetic eddies are generated inside the region containing slowly moving fluid in between this SSL and the South Bank.

The free-surface, mean vorticity distribution in the  $VR=0.08$ ,  $Ri=1.89$  case (Fig. 2b) is qualitatively more similar to the one observed in the corresponding no-density-effects case (Fig. 2a) rather than the one predicted in the  $VR=0.41$ ,  $Ri=0.67$  case (see [11]). This is not surprising given that the temperature difference between the two streams, though of comparable magnitude, is of opposite signs in the two simulations with  $Ri > 0$ . As the Richardson number increases from 0 to 1.89 in the  $VR=0.08$  simulations, the SSL forming on the Ebro River side of the confluence apex is pushed laterally toward the Segre River channel. As will be discussed later, the sudden width increase near its end is due to the quasi-periodic formation and shedding of large eddies from its end. Similar to the  $Ri=0$  simulation, a thick band of relatively high vorticity forms downstream of the very energetic part of this SSL. Though, the thickness of this region is also close to  $35D$  around sections B and C in the  $VR=0.08$   $Ri=1.89$  case, this region is situated farther away from the centerline of the main channel compared to the corresponding no-density-effects simulation and touches the North Bank around section C. Its thickness is less than  $15D$  past section D. Close to the free surface, the SSL forming at the South Bank near section A is shorter and much less energetic compared to the no-density-effects case (Fig. 2a). A main feature of the free-surface, mean streamline patterns in Fig. 2b is the formation of a large recirculation bubble near the confluence apex that penetrates until the opposing North Bank and extends into the Segre River channel. Its formation is a direct consequence of the rapid plunging of denser fluid from the Segre River (the denser fluid is drawn toward the confluence apex, away from the North Bank) and the free surface expansion of less-dense fluid from the Ebro River.

The mean streamwise velocity distribution in the  $VR=0.08$ ,  $Ri=0$  case (Fig. 3a) is qualitatively similar to that observed in the other no-density-effects ( $VR=0.41$ ,  $Ri=0$ ) case (see Fig. 5a in [11]). In both simulations, as one moves in the downstream direction, the core of high velocities from the Ebro River side of the main channel gradually approaches the North Bank. The lateral movement of the core is larger in the  $VR=0.08$ ,



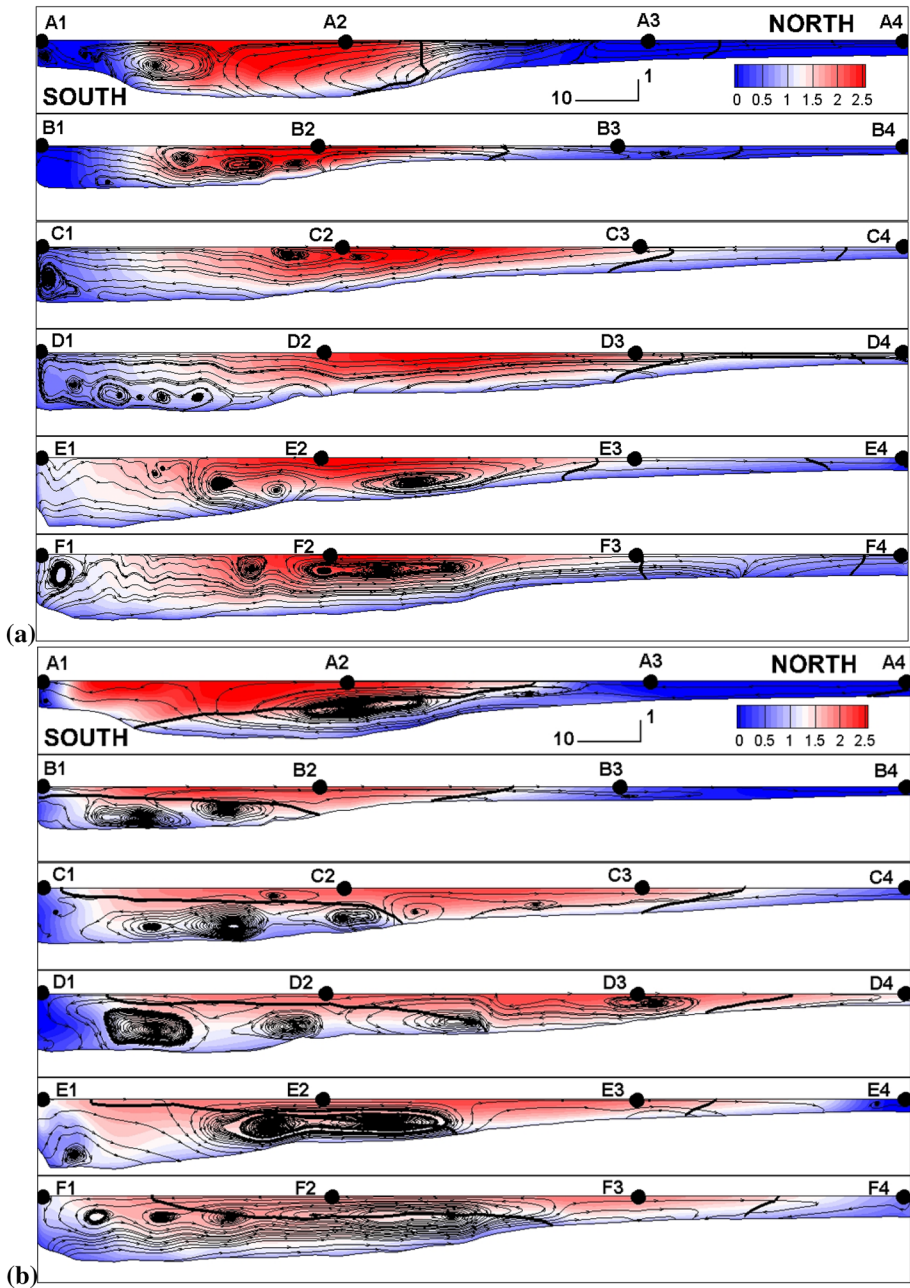


**Fig. 3** Distribution of streamwise velocity,  $u/U_0$ , and 2D streamline patterns at cross-sections A to F in the mean flow. **a**  $Ri=0$ ; **b**  $Ri=1.89$ . The solid black lines ( $C'=0.1$  and  $C'=0.9$ ) visualize the edges of the MI region based on the distribution of  $C'$  in the mean flow field

$Ri=0$  simulation, which is somewhat expected given the much larger difference between the discharges of the two tributaries in this case. The MI, defined as the region with  $0.1 < C' < 0.9$ , also moves faster toward the South Bank in the  $VR=0.08$   $Ri=0$  simulation such that the MI is situated in its entirety over the shallower part of the main channel past section D. By contrast, part of the MI is always situated over the transition region between the deeper South Bank side and the shallower North Bank side of the main channel in the  $VR=0.41$ ,  $Ri=0$  case. In both no-density-effects simulations, most of the cross-stream eddies of secondary flow are situated over the deeper part of the main channel, outside of the MI region.

The distribution of the streamwise momentum inside the confluence hydrodynamic zone is very different in the  $VR=0.08$ ,  $Ri=1.89$  (Fig. 3b) simulation compared to the corresponding no-density case (Fig. 3a). This is mainly because of the very large re-distribution of the streamwise momentum starting immediately downstream of the confluence apex in the simulation with strong flow stratification. The heavier fluid from the Segre River advected close to the bank containing the confluence apex plunges beneath the free surface as it passes the apex and then advances across the Ebro River side of the main channel beneath the core of high-speed, less-dense fluid from the Ebro River that moves downstream without much change in its direction. This generates a two-layer vertical flow structure close to the confluence apex with the denser fluid moving beneath the less-dense fluid. One should also note that bed morphology at the present confluence where there is a cross-sectional (transverse) slope from the North Bank to the South Bank is not creating obstacles to the intrusion of the denser fluid below the Ebro waters. Hence, this flow patterns should be common in confluences with bed discordance and significant density differences, if the denser water is in the shallower tributary.

The dominant mean flow directions of the flows originating in the two tributaries are close to perpendicular to each other (see also discussion of Figs. 8b and 9b). This is the main reason why at section A, that is situated only 40D from the confluence apex, the interface with the unmixed less-dense fluid has a fairly small inclination with respect to the horizontal and penetrates until close to the South Bank (Fig. 3b). The denser fluid originating in the Segre River resembles a bottom intrusion at section A. The difference with the classical time-developing bottom propagating gravity current is that the intrusion does not grow in time. Once the denser fluid moving near the bed reaches the South Bank it rotates and then follows the South Bank. This explains the formation of the second density interface over the deep side of the main channel starting with section B (Fig. 3b). One should mention that a similar situation was observed at the confluence between Río Bermejo and Río Paraguay [4]. The core of high streamwise velocities containing less dense fluid from the Ebro River moves over the region situated in between the shallower and the deeper parts of the cross section. By section C, the core of high streamwise velocity, less-dense fluid is situated in between two regions containing denser, slower fluid. As one moves downstream, the core of relatively high streamwise velocities penetrates closer to the South Bank and increases its vertical thickness over the deeper side of the cross section. Such a flow distribution is impossible to form inside the confluence hydrodynamic zone in the absence of strong density difference effects. In the  $VR=0.41$ ,  $Ri=0.67$  case [11] the interface between the regions containing denser fluid and less-dense fluid became strongly tilted due to the lateral intrusions of denser fluid near the bed and of less dense fluid near the free surface. However, no dense fluid was able to penetrate close to the opposite bank such that the less dense fluid will be bordered by mixed denser fluid on its two sides. This is a major difference between the two cases with  $Ri \gg 0$ .

In terms of the secondary flow, several cross-stream eddies are observed at most sections in the  $VR=0.08$ ,  $Ri=1.89$  case (Fig. 3b). Most of these eddies are situated along or immediately beneath the interface between the fairly unmixed, less-dense fluid originating in the Ebro River tributary and the mixed fluid originating in the Segre River tributary that is moving with the near-bed intrusion toward the South Bank. These eddies resemble the ones forming around the interface between the near-bed and free-surface gravity currents in a classical lock-exchange flow. Thus, for the strong density difference conditions present in this case, stratification controls not only the redistribution of the streamwise momentum but also the formation of the main secondary-flow eddies.

## 5 Flow structure near the confluence apex and inside the mixing interface region

Similar to what was observed for the no-density-effects ( $VR=0.41$ ,  $Ri=0$ ) case investigated by Cheng and Constantinescu [11], energetic KH billows are generated over the upstream part of the SSL forming on the Ebro River side of the confluence apex in the  $VR=0.08$ ,  $Ri=0$  case. The average size of these billows is close to  $3\text{--}4 D$ . Then, these billows merge into a much larger eddy that is advected inside the MI. The mean period associated with the formation of a new large eddy is about  $40D/U_0$  in the  $VR=0.41$ ,  $Ri=0$  case and  $55D/U_0$  in the  $VR=0.08$ ,  $Ri=0$  case. However, no SSL forms on the Segre River side of the confluence apex and no wake region is present in the  $VR=0.08$ ,  $Ri=0$  simulation. Rather, part of the flow moving in the Segre River close to the bank containing the apex reaches the SSL on the Ebro River side and then changes direction as it is advected into the MI region. This sudden change in direction is associated with the formation of the large eddy containing vorticity from the SSL. The frames between  $t=t_0$  and  $t_0+45D/U_0$  in Fig. 4 illustrate the formation of the large eddy in which the KH billows from the SSL are drawn into before it separates. Then this eddy moves along the interface with the unmixed fluid from the Segre River before it starts dissipating while being advected downstream. A new eddy starts forming at  $t=t_0+45D/U_0$ . At  $t=t_0+55D/U_0$  the old eddy has disappeared and the flow pattern is similar to the one observed at  $t=t_0$  (Fig. 4). The vorticity plots in Fig. 4 also show that two large eddies are present at most times in between the South Bank and the SSL forming upstream of section A. These eddies interact with the SSL. Strong interactions are also observed in between the turbulent eddies generated by the streamwise oriented ridge present in the Ebro River tributary with eddies advected inside the SSL forming at the South Bank.

Flow stratification acts very differently in the case where the higher-temperature stream containing less dense fluid corresponds to the main, high-discharge tributary and in the case the lower temperature stream corresponds to the high-discharge tributary. In the latter case (e.g., see results for the  $VR=0.41$ ,  $Ri=0.67$  case in [11], no large-scale, quasi-periodic motions were observed within the confluence hydrodynamic zone aside from eddies shed in the SSLs and near the bank lines. This is not the case in the  $VR=0.08$ ,  $Ri=1.89$  simulation, where a large unsteady recirculating flow bubble forms near the free surface in between the region containing unmixed denser fluid from the Segre River and the high-speed, less dense fluid from the Ebro River (see 2-D streamline patterns in Fig. 2b). Once it forms, this bubble increases its size and eventually moves toward the North Bank, while a new bubble starts forming behind it (Fig. 5). The 2-D free-surface flow patterns in Figs. 2b and 5 suggest that all the incoming flow from the Segre River is moving toward the

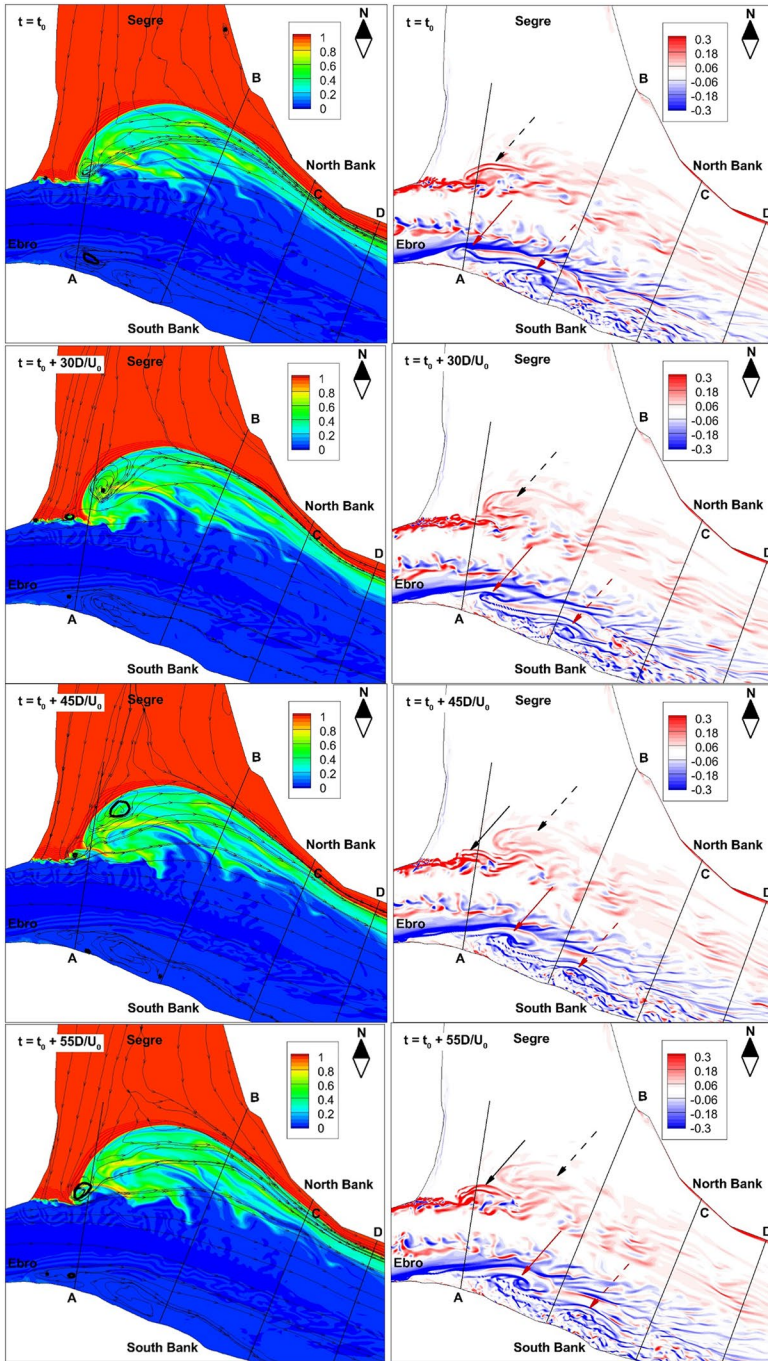
**Fig. 4** Visualization of mixing between the two streams and large-scale turbulence for the  $Ri=0$  case. The concentration of the passive scalar is  $C'=1$  at the inlet of the Segre River channel and  $C'=0$  at the inlet of the Ebro River channel. The instantaneous concentration,  $C'$ , (left frames) and vertical vorticity,  $\omega_z D/U_0$ , (right frames) fields are shown in a horizontal plane ( $z/H=-0.1$ ) situated near the free surface. The black arrows track the large vortical structures forming from the merging of co-rotating eddies shed from the separated shear layer on the Ebro River side of the confluence apex. The red arrows track the large vortical structures in the region containing slowly moving fluid forming near the South Bank

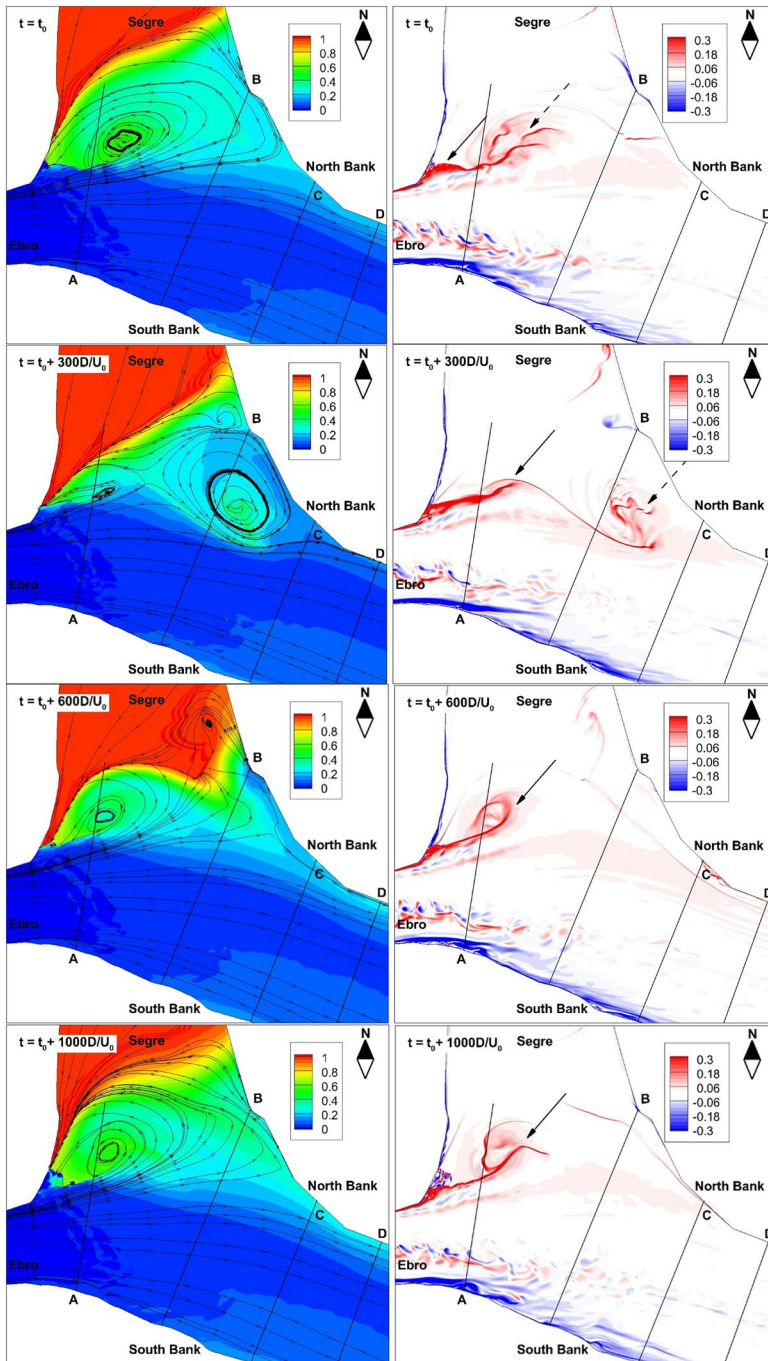
recirculation bubble and from there the flow is drawn toward the confluence apex, which is misleading. In reality, the mean flow is highly three-dimensional in the region where the two streams come into contact with the mean flow patterns being very different close to the free surface and close to the bed. The denser fluid situated close to the bank containing the apex starts plunging downwards as it approaches the apex. Close to the bed, there is a corridor containing fluid from the Segre River that is advected across the main channel and reaches the South Bank (Fig. 9b).

At peak size, the unsteady bubble occupies the whole triangular region containing mixed fluid near the end of the Segre River tributary channel (e.g., see frame at  $t=t_0$  in Fig. 5). The bubble forms close to the confluence apex in the region of high mean shear between the fast moving fluid from the Ebro River that advances in the main channel and the fluid from the Segre River which converges toward the confluence apex. A new bubble starts forming around  $t=t_0+300D/U_0$  (Fig. 5). As the new bubble forms, the old one moves toward the North Bank. Its core becomes smaller and starts interacting with the boundary layer forming at the North Bank. Then, the core of the old bubble is advected parallel to the North Bank. At the same time, mixing near the free surface is strongly enhanced as denser fluid from inside the bubble mixes with the surrounding less dense fluid (see nondimensional density plot at  $t=t_0+300D/U_0$  in Fig. 5). Once it reaches the North Bank, the bubble starts dissipating and loses its coherence over the next  $200D/U_0$  (see results for  $t=t_0+600D/U_0$  in Fig. 5). Meanwhile, the new eddy reaches maximum size around  $t=t_0+1000D/U_0$  (Fig. 5). It then takes another  $100D/U_0$  until the interface with the unmixed heavier fluid assumes a shape that is similar to the one observed at  $t=t_0$ . So, the period associated with a complete cycle is around  $1000-1100D/U_0$ , more than one order of magnitude larger compared to the large-scale unsteadiness observed in the  $VR=0.41$ ,  $Ri=0.67$  case and the no-density-effects cases.

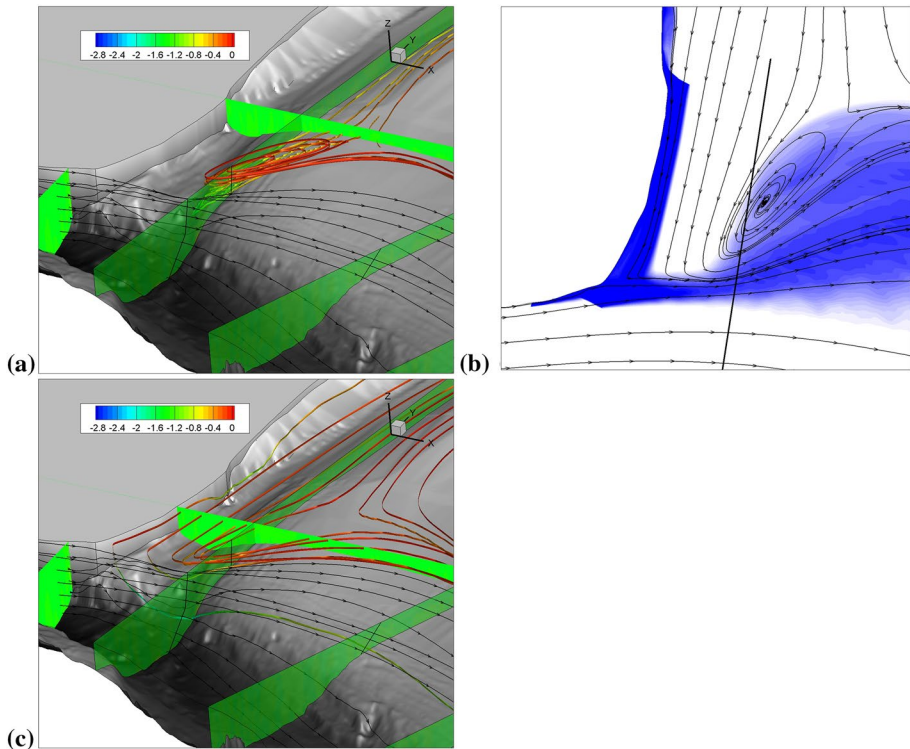
Compared to the  $VR=0.08$ ,  $Ri=0$  case (Fig. 4), the flow separation region at the South Bank in the  $VR=0.08$ ,  $Ri=1.89$  case is much reduced. This may look surprising given that the incoming flow velocity in the Ebro River is about the same in both simulations. The reason is that for strong stratification the denser fluid from the Segre River moving toward the South Bank plunges toward the bed and once it gets close to the South Bank starts moving approximately parallel to the bank line. Mixing takes place and this denser fluid reaches the free surface downstream of section B. This explains the presence of mixed fluid close to the South Bank in the non-dimensional density fields shown in Fig. 5.

Figure 6 visualizes the mean flow pattern in the  $VR=0.08$ ,  $Ri=0$  simulation close to the confluence apex and the trajectories followed by fluid particles originating in the two channels. Some of the streamlines originating close to the free surface in the Segre River channel and approaching the confluence apex are entrained into the mean-flow recirculation bubble. Others are moving around the bubble and are then advected inside the mixing interface region close to the free surface (see Fig. 6b and red ribbons Fig. 6c). The streamlines originating close to the bed in the Segre River channel (see red ribbons in Fig. 6a) are first entrained into the recirculation bubble and then move toward the free surface inside





**Fig. 5** Visualization of mixing between the two streams and large-scale turbulence for the  $Ri = 1.89$  case. The non-dimensional temperature is  $C' = 1$  at the inlet of the Segre River channel and  $C' = 0$  at the inlet of the Ebro River channel. The instantaneous nondimensional temperature,  $C'$ , (left frames) and vertical vorticity,  $\omega_z D/U_0$ , (right frames) fields are shown in a horizontal plane ( $z/H = -0.1$ ) situated near the free surface. The black arrows track the advection toward the North Bank of large recirculation bubbles forming near the confluence apex



**Fig. 6** Visualization of mean flow pattern close to the confluence apex using 3D streamlines for the  $Ri=0$  case. The streamlines originate in the Ebro River close to the bank containing the confluence apex (black lines) and in the Segre River, close to the free surface (colored ribbons). Frame **a** illustrates how particles from the Segre River are drawn into the recirculation bubble forming close to the confluence apex. Frame **b** shows the concentration distribution close to the confluence apex for a passive scalar introduced near the apex. Frame **c** illustrates how particles originating in the Ebro River move over the North Bank side of the main channel, while some of the particles originating in the Segre River move in between the recirculation bubble and the bank containing the confluence apex before moving back on the North Side of the main channel. Ribbons' color and legend indicate vertical elevation. (Aspect ratio  $X:Y:Z=10:10:1$ )

the core of this eddy before being released into the mixing interface region. On the Ebro River side of the confluence, 3-D streamlines released close to the bank and near the bed move around the recirculation eddy and closer to the free surface as they approach the SSL forming on the Ebro River side of the confluence apex (Fig. 6). Most of the streamlines dive down as they pass the confluence apex and then they increase their elevation as they migrate over the shallower regions of the main channel while remaining fairly close to the channel bottom. Meanwhile, the 3D streamlines released close to the bank containing the confluence apex and near the free surface remain on the South Bank side of the main channel.

Compared to the no-density-effects case, the degree of flow three dimensionality in the region surrounding the confluence apex is much higher in the  $VR=0.08$ ,  $Ri=1.89$  simulation where fluid particles released in each of the two incoming channels can move on the other side of the main channel. 3D streamlines released close to the free surface and the bank containing the confluence apex inside the Ebro River channel (red ribbons in Fig. 7a)

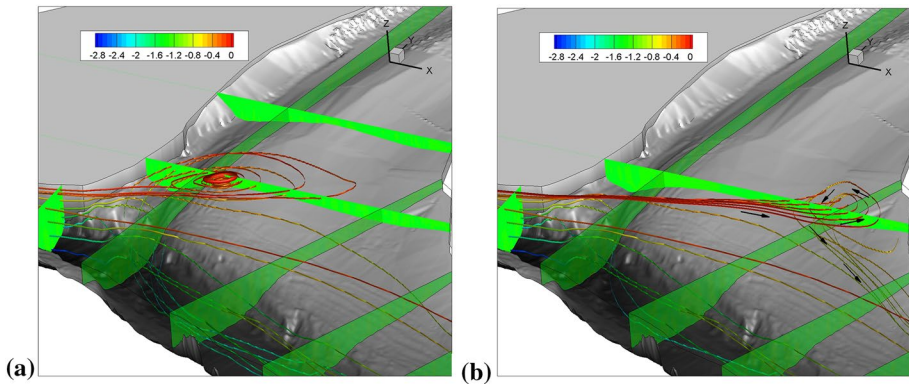


**Fig. 7** Visualization of mean flow pattern close to the confluence apex using 3D streamlines for the  $Ri = 1.89$  case. Frames **a** visualizes the main recirculation bubble forming near the confluence apex and how some fluid particles originating in the Segre River reach the region situated close to the South Bank. Frame **b** visualizes the flow pattern around the submerged recirculation bubble present close to the North Bank. Ribbons' color and legend indicate vertical elevation. (Aspect ratio X:Y:Z = 10:10:1)

are first entrained into the core of the main recirculation bubble and from there they move downwards inside the core of this tornado-like eddy before being released into the deeper South Bank side of the main channel. Meanwhile, 3D streamlines released at mid-depth levels and close to the bed are not entrained into the recirculation bubble and follow the deeper part of the South Bank side of the main channel. A unique feature of the mean flow field for this case is that a second recirculation eddy is present beneath the free surface, close to the region where the North Bank line changes direction (Fig. 7b). Some of the streamlines released close to the free surface inside the Ebro River channel that are not entrained into the main recirculation bubble are moving past this eddy and are entrained into the recirculation eddy forming close to the North Bank. These particles are then moving toward the bed inside the core of the second recirculation eddy and are then released into the flow being advected close to the North Bank (red ribbons in Fig. 7b). Most flow particles released in the Segre River channel plunge down as they approach the main recirculation bubble and then move close to the bed until they reach the South Bank.

## 6 Mixing

In the  $VR = 0.08$ ,  $Ri = 0$  case, the free-surface, vertical vorticity distributions in the instantaneous flow fields (Fig. 4) show that large-scale, energetic eddies that were not entrained into the main recirculation bubble are moving along the interface between the high velocity fluid originating in the Ebro River and the region containing mixed fluid ( $0.1 < C' < 0.9$ , Fig. 8a). These eddies enhance mixing mostly via engulfing and are the main mechanism for mixing close to the free surface. By contrast, the instantaneous flow fields contain a much lesser amount of energetic eddies close to the interface between the unmixed fluid originating in the Segre River and the region containing mixed fluid.

Despite the relatively large degree of bed discordance, the mean flow and mixing patterns are qualitatively very similar near the free surface (Fig. 8a) and near the bed



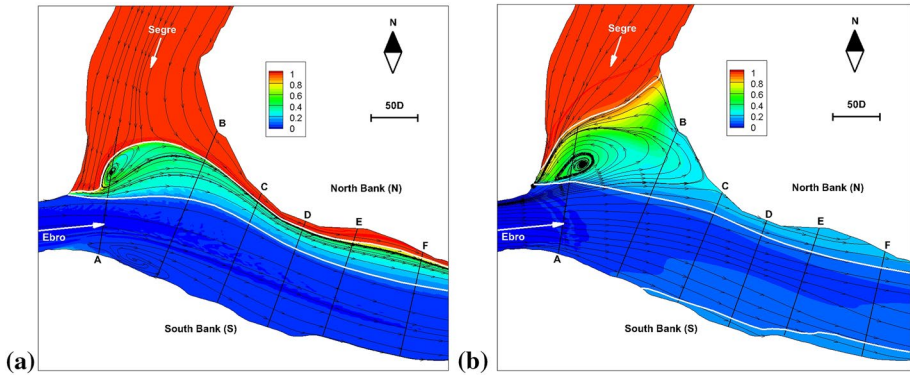


**Fig. 8** Visualization of mixing between the two streams in the mean flow using the non-dimensional temperature field,  $C'$ . The temperature field is shown in a horizontal plane ( $z/H = -0.1$ ) situated near the free surface. **a**  $Ri=0$ ; **b**  $Ri=1.89$ . The white lines visualize the edges of the regions containing mixed fluid ( $C'=0.1$  and  $C'=0.9$ ) in the mean flow. Also shown are 2D streamlines

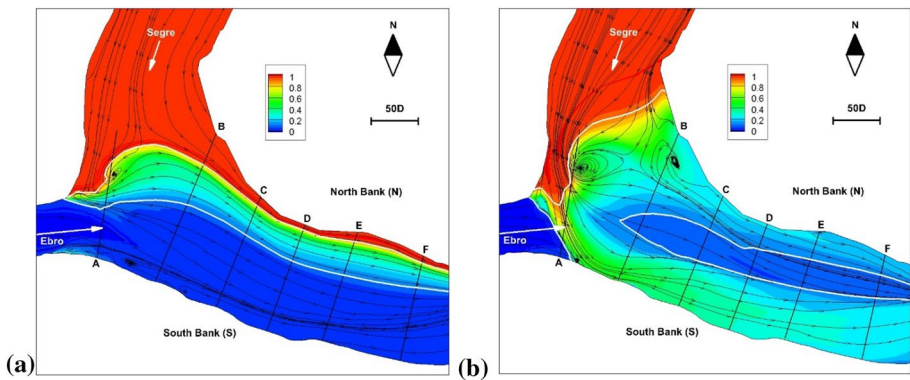


**Fig. 9** Visualization of mixing between the two streams in the mean flow using the non-dimensional temperature field,  $C'$ . The temperature field is shown in a deformed plane situated near the bed at a distance of about  $0.1D$  from the bed surface. **a**  $Ri=0$ ; **b**  $Ri=1.89$ . The white lines visualize the edges of the regions containing mixed fluid ( $C'=0.1$  and  $C'=0.9$ ) in the mean flow. Also shown are 2D streamlines

(Fig. 9a) in terms of the 2D streamline patterns, the position of the main recirculation bubble and the position of the region containing mixed fluid ( $0.1 < C' < 0.9$ ). The recirculation bubble is larger near the free surface, while the width of the region containing mixed fluid is larger near the bed. The cross section distributions of  $C'$  in the mean flow fields (Fig. 10a) show that the MI moves over the shallower parts of the main channel downstream of section A1. Near-bed intrusions of mixed fluid into the Ebro River side of the main channel are observed only close to the confluence apex (e.g., see results for section A in Fig. 10a) on the Ebro River side of the main channel where the flow is highly three dimensional due to the strong bed discordance.

By contrast, the density distributions near the free surface (Fig. 8b) and near the bed (Fig. 9b) are very different in the  $VR=0.08$ ,  $Ri=1.89$  case. These differences are driven by the near-bed current that transports denser fluid from the Segre River. Close to the

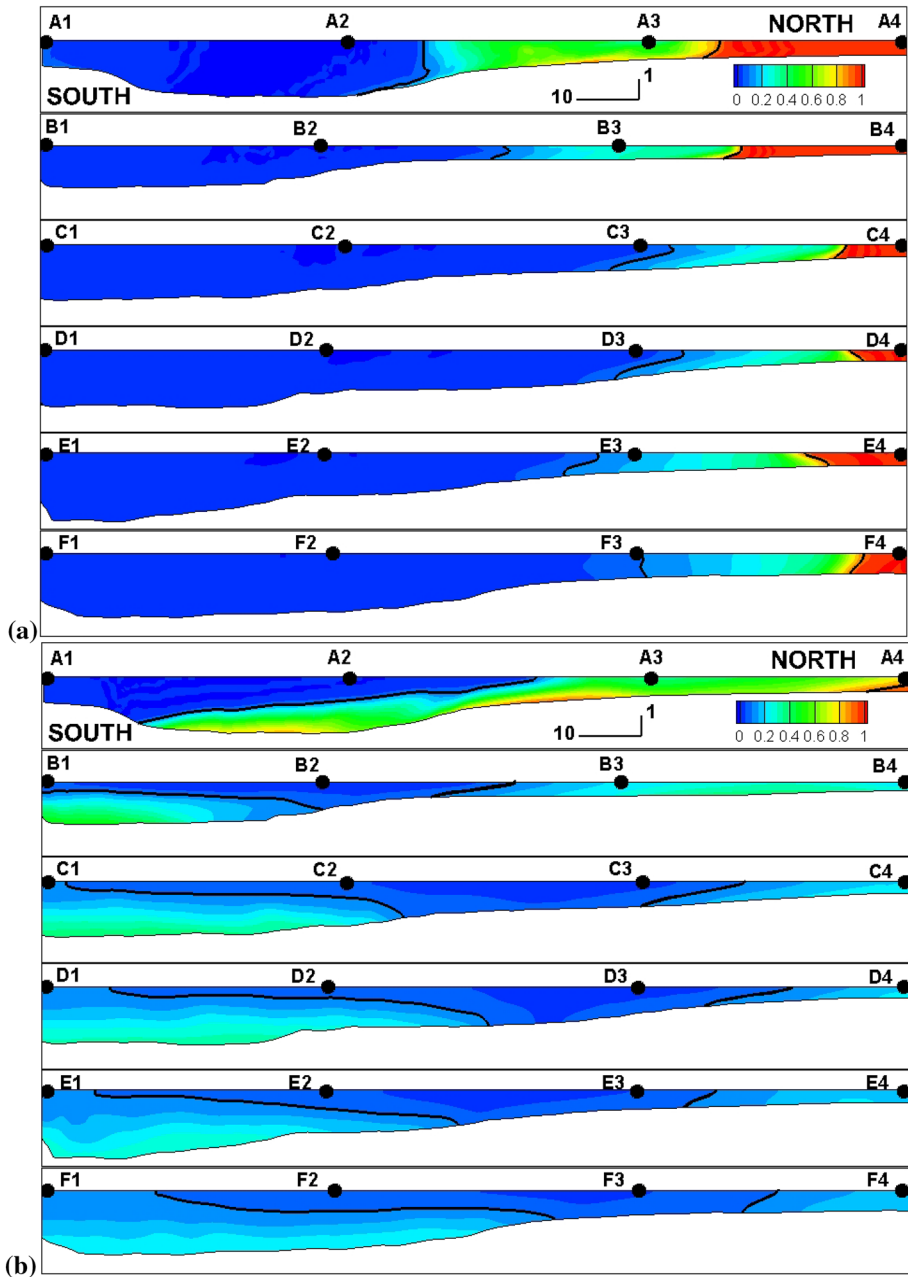


**Fig. 10** Distribution of non-dimensional temperature,  $C'$ , at cross-sections A to F in in the mean flow. **a**  $Ri = 0$ ; **b**  $Ri = 1.89$ . The solid black lines ( $C' = 0.1$  and  $C' = 0.9$ ) visualize the edges of the regions containing mixed fluid in the mean flow

free surface, the denser fluid from the Segre River starts plunging toward the bed as it approaches the main recirculation bubble and, at the same time, is pushed toward the bank containing the confluence apex. Upstream of the confluence apex, the near-bed current extends for about  $30D$  away from the Segre River bank containing the confluence apex (Fig. 9b). From there, the near-bed current moves toward the South Bank that is reached in between sections A and B. Then, the current is deflected by the bank line and flows parallel to it. As this is a shallow area and the current expands in both the lateral and vertical directions, the nondimensional temperature/density levels near the free surface show the presence of mixed fluid near the South Bank downstream of section C (Fig. 8b). The free-surface distribution of  $C'$  downstream of section C, contains three regions. The region containing the least dense fluid is bordered by regions containing denser fluid. Such a lateral distribution of the free surface mixing is a direct consequence of strong stratification and associated 2-layer vertical flow structure observed near the confluence apex. Such free-surface mixing patterns are impossible to observe at confluences where density difference effects are small or negligible.

Due to the near-bed current of denser fluid moving across the Ebro River side of the main channel, the 2D streamline patterns are very different close to the bed (Fig. 8b) and the free surface (Fig. 9b). A secondary recirculation bubble is present close to the bed and, as discussed, plays an important role in vertical transport inside the main channel. The formation of this cell is mostly due to the complex bathymetry and the vertical flow nonuniformity induced by the free-surface intrusion of lighter, mixed fluid into the Segre River tributary. This intrusion is associated with the development of buoyancy effects (e.g., the lock-exchange flow). The core of this eddy transports mixed fluid from the free surface toward the bed and from there into the near-bed region containing mixed fluid that moves parallel to the North Bank. Meanwhile, the less-dense fluid from the Ebro River moving close to the bed is advected upwards toward the free surface as it moves over the cross-stream, near-bed current containing denser fluid and then gradually expands vertically toward the bed. This explains the presence of a region containing less-dense fluid near the centerline of the main channel downstream of section B in Fig. 9b.

The distribution of  $C'$  at section A visualizes the developing intrusion of denser fluid from the Segre River as it plunges down at the end of the shallower region to form the near-bed current. The current has completed its turn by section B where the mixed fluid penetrates until the South Bank. As one moves downstream, this current extends vertically upwards and laterally toward the North Bank. The large cells of secondary flow present in sections B and F (Fig. 3b) near the interface between the current containing denser fluid and the surrounding less dense fluid from the Ebro River are the main reason for the growth of the current in the cross-stream direction as one moves downstream. Finally, the tilting of the interface between the less dense fluid from the Ebro River and the denser Segre River fluid moving close to the South Bank is due to the spatial development of a lock-exchange like flow. The main difference with the stratified flow ( $VR=0.41$ ,  $Ri=0.67$ ) case discussed by Cheng and Constantinescu [11] is that the lock-exchange-like flow developed on the South Bank side of the main channel and that no fluid from the Segre River could penetrate to the South Bank. This is why the free-surface distribution of  $C'$  contained only two regions in the downstream part of the main channel.

Figure 11 compares the streamwise evolution of the volume of mixed fluid, defined as fluid with  $0.1 < C' < 0.9$ , in the  $VR=0.08$ ,  $Ri=0$  and  $VR=0.08$ ,  $Ri=1.89$  cases. The rate of growth of the volume of mixed fluid is much larger in the  $Ri=1.89$  simulation. For example, the ratio between the volume of mixed fluid in the two cases is about 3.2 at section C ( $x'/D=180$ ) and about 4 at section F ( $x'/D=370$ ). This means the two

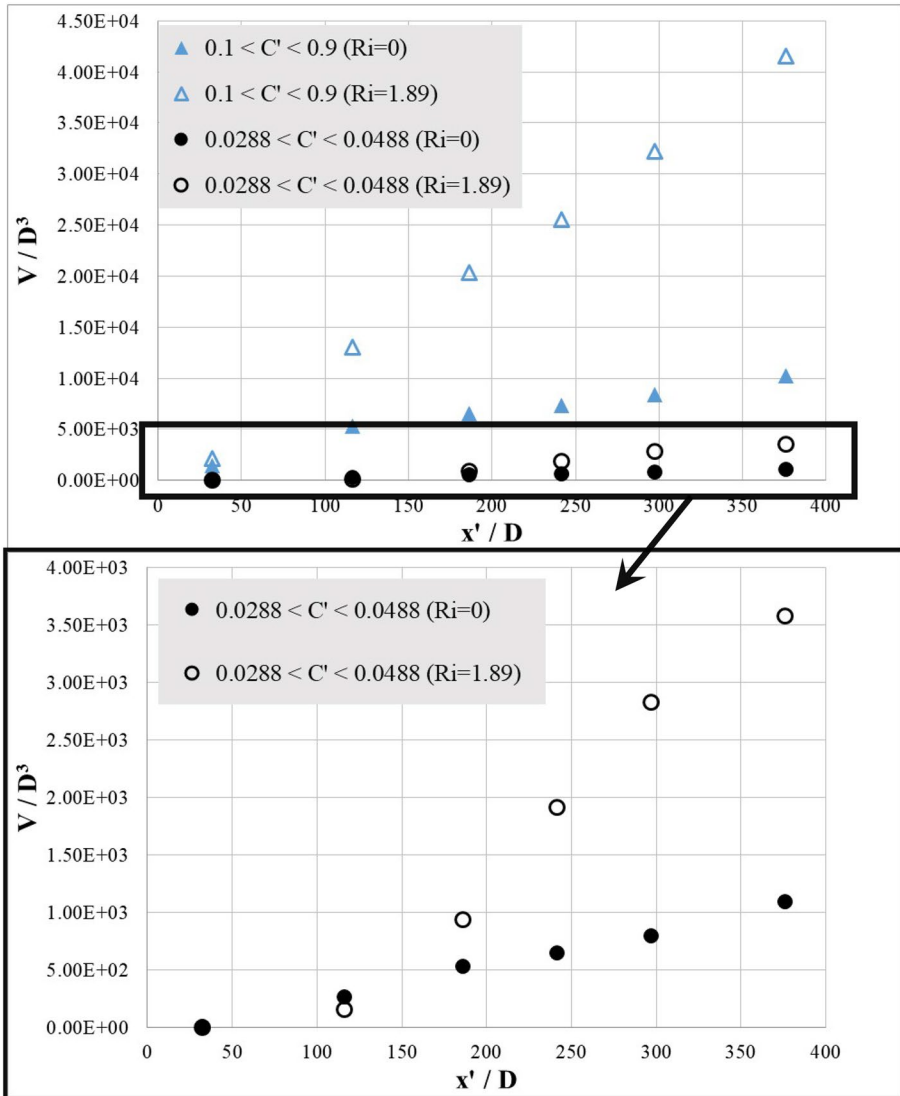


**Fig. 11** Comparison of mixing for the  $Ri=0$  and  $Ri=1.89$  cases. **a** Streamwise variation of the non-dimensional volume of mixed fluid,  $V/D^3$ . The mixed fluid is defined as fluid with  $0.1 < C' < 0.9$  (blue symbols) and also as fluid with  $0.0288 < C' < 0.0488$  (black symbols), where  $C'_{\text{mixed}}=0.0388$  is the nondimensional temperature expected in the main channel after the two streams are fully mixed. The coordinate  $x'$  is measured along the centerline of the MI at the free surface with  $x'=0$  at the confluence apex

incoming streams will become fully mixed much faster in the  $Ri=1.89$  simulation compared to the  $Ri=0$  simulation.

The much stronger mixing observed in the  $VR=0.08$ ,  $Ri=1.89$  simulation is due to several reasons. The first one is the unsteady dynamics associated with the quasi-periodic generation of large recirculation bubbles close to the confluence apex. These bubbles engulf

less dense fluid from the Ebro River. The second one is the formation of a near-bed current of denser fluid that is advected toward the South Bank. Due to large interfacial shear, mixing takes place in between this current and the surrounding less-dense fluid. Moreover, the very energetic eddies generated near the South Bank side of the main channel are also very effective in increasing mixing especially as the current of denser fluid approaches the bank and then moves parallel to it.

Also shown in Fig. 11 is the streamwise variation of the volume of ‘well-mixed’ fluid, that is defined as fluid with a nondimensional temperature/density  $0.0288 < C' < 0.0488$ , close to the value,  $C'_{\text{mixed}} = 0.0388$  corresponding to the two streams being fully mixed.  $C'_{\text{mixed}}$  is calculated as a weighted average of  $C'$  in the two incoming streams, with the relative discharges in the two streams as the weights. The detailed view in Fig. 11 shows that, at large distances from the confluence apex, the rate of growth of the volume of well-mixed fluid is also much larger in the simulation with strong density differences between the incoming flows. For example, the ratio of the volume of well-mixed fluid in the  $VR=0.08$ ,  $Ri=1.89$  case to that in the  $VR=0.08$ ,  $Ri=0$  case is close to 3.5 at section F ( $x'/D=370$ ). The only qualitative difference with the streamwise variation of the volume of mixed fluid is that the volume of well-mixed fluid is slightly larger in the no-density-effects case close to the confluence apex.

Compared to the  $VR=0.41$  simulations discussed in Cheng and Constantinescu [11] for which the Ebro River tributary contained the denser fluid, the trends observed in the streamwise variations of the volumes of mixed and well-mixed fluids are different. In the  $VR=0.41$  simulations, the volumes of mixed and well-mixed fluid are smaller in the no-density-effects case close to the confluence apex, but their rates of growth are slightly larger such that by section F the two volumes are relatively close in the  $VR=0.41$ ,  $Ri=0$  and  $VR=0.41$ ,  $Ri=0.67$  simulations. This shows that the way stratification induced by density differences between the incoming flows affects mixing within and downstream of the confluence hydrodynamic zone is not solely a function of the magnitude of the Richardson number. The density ratio between the faster and the slower stream and the velocity/momentum ratio of the incoming streams can strongly affect how mixing develops away from the confluence apex, at least for confluences with a large degree of bed discordance.

## 7 Turbulent kinetic energy

The passage or presence of large-scale vortical eddies generated by Kelvin–Helmholtz instabilities, flow separation, large-scale features of the bathymetry and rapid changes in the bank line orientation is the main mechanism responsible for the production of turbulent kinetic energy (TKE) inside the confluence hydrodynamic zone.

Two main region of high (depth-averaged) TKE are present in the  $VR=0.08$ ,  $Ri=0$  simulation (Fig. 12a). The first region corresponds to the SSL on the Ebro River side of the confluence apex and to the adjacent region where large eddies are shed quasi periodically (see vorticity distributions in Fig. 4). The second region is centered around the upstream part of the SSL forming at the South Bank, where the bank line changes orientation and the flow advected in the Ebro River separates. The instantaneous vorticity distributions in Fig. 4 show that the region situated in between this SSL and the South Bank contains lots of energetic eddies which explain the relatively high TKE levels ( $k/U_0^2 > 0.02$ ) present for a distance of about  $20D$ – $25D$  away from the South Bank, downstream of section A. The ridge associated with the sudden change in bed elevation inside the Ebro River tributary

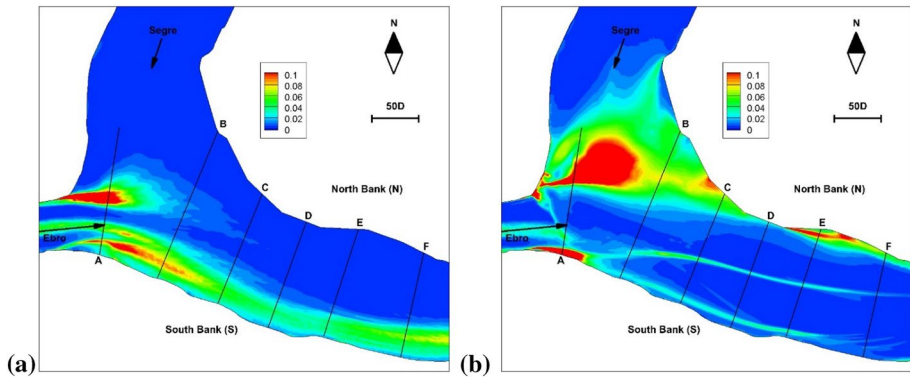


**Fig. 12** Distribution of the depth-averaged TKE,  $k/U_0^2$ . **a**  $Ri=0$ ; **b**  $Ri=1.89$

(Fig. 1) is another source of energetic eddies (Fig. 4) and explains the presence of the second streak of high TKE parallel to the region of high TKE associated with the SSL forming upstream of section A (Fig. 12a).

The depth-averaged TKE distribution in the  $VR=0.08$ ,  $Ri=1.89$  case (Fig. 12b) presents several important differences compared to the one observed in the no-density-effects case (Fig. 12a). One main difference is the larger region of high TKE corresponding to the SSL forming on the Ebro River side of the confluence apex and to the recirculation bubbles that are shed quasi-periodically. The largest TKE amplification is observed inside the core of this bubble based on its mean-flow location (Fig. 8b) and in the region where these eddies reach the North Bank, just upstream of section C. The other region of high TKE values is situated at the South Bank and is centered around section A. Though the high bank curvature is partially responsible for the TKE increase, the main reason for the turbulence amplification is the interaction of the near bed current containing denser fluid with the South Bank (Fig. 9b). Two long streaks of relatively high TKE are also forming on the South Bank side of the main channel. The one in the middle of the channel is associated with the interface forming between the high-speed, less-dense fluid originating in the Ebro River and the slower, but denser fluid from the near-bed current that, after it reaches the bank, moves parallel to it. Most of the TKE amplification occurs because of transverse oscillations of the interface around its mean flow position. The other streak of high TKE corresponds to the shear layer forming in the immediate vicinity of the irregular bank line (Fig. 2b) where flow separation occurs at several locations. A similar shear layer forms in the mean flow at the North Bank downstream of section D and is responsible for the high TKE amplification in that region (Fig. 12b).

## 8 Bed shear stresses

Confluent flows are characterized by the generation and advection of large-scale coherent structures near the bed. This is why when estimating the capacity of the flow to entrain sediment, besides the mean bed shear stress magnitude,  $\tau$ , one also has to consider information on the fluctuations of this variable due to turbulence. In a first approximation, the effect of the coherent structures can be quantified by analyzing the distributions of the root-mean-square (rms) of the bed shear stress,  $\tau^{\text{rms}}$  [12]. Given that the first grid point off the

channel bed is situated at 2–3 wall units, the mean bed shear stress is calculated using the definition and the mean velocity magnitude in a plane parallel to the tangent plane to the bed surface passing through the first grid point off the bed. To calculate  $\tau^{\text{rms}}$ , the velocity magnitude is replaced by the square root of the turbulent kinetic energy at the first grid point off the bed surface. The bed surface is rocky but one of the tributaries advects fine sediments with a mean diameter of about 30  $\mu\text{m}$ . These fine sediments can deposit or be re-entrained by the flow.

As for the no-density-effects VR=0.41 simulation [11], regions of high  $\tau$  in in the VR=0.08, Ri=0 case (Fig. 13a) correspond to regions of large streamwise velocity (Fig. 3a). Given the high mean velocity of the flow in the Ebro River, the largest bed shear stresses are induced over the deep part of this incoming channel and then over the deepest parts of the main channel close to the South Bank. The width of the region of relatively high  $\tau$  increases downstream of section A as the core of high velocity from the Ebro River tributary enlarges and gradually moves over the region where the bathymetry transitions from the deeper South Bank side toward the much shallower North Bank side (Fig. 3a).

In the VR=0.41, Ri=0 case, the largest  $\tau^{\text{rms}}$  values are predicted beneath the regions where KH billows are shed inside the SSL forming at the South Bank upstream of section A (Figs. 4a and 14a). Two other regions of significantly larger  $\tau^{\text{rms}}$  compared to values associated with the fully turbulent flow in the incoming channels are present. The first one corresponds to the SSL forming at the confluence apex on the Ebro River side inside which KH billows are shed and merge to form large eddies. The second one corresponds to the end of the elongated ridge inside the Ebro River channel where energetic vortical eddies are shed toward the SSL forming at the South Bank (Fig. 4a).

For the conditions considered in this case, the erosive capacity of the flow is the largest in the region situated close to the South Bank, between section A and B, where both  $\tau$  and  $\tau^{\text{rms}}$  are close to their peak values. This conclusion is similar to the one reached for the other no-density-effects (VR=0.41, Ri=0) case. This region of high  $\tau$  and  $\tau^{\text{rms}}$  does not penetrate to the bank line (Figs. 13a, 14a), so erosion at the South Bank is not expected to be a concern for this case. Meanwhile, the very low values of  $\tau$  and  $\tau^{\text{rms}}$  near the North Bank, between sections E and F, suggest that sediment deposition may occur over this region if the incoming streams contain sediment.

Downstream of the confluence apex, the distribution of  $\tau$  in the VR=0.08, Ri=1.89 case (Fig. 13b) is very different from the one observed in the corresponding no-density-effects case and also from the one observed in the stratified flow (VR=0.41, Ri=0.67) case where the Ebro River contained the denser fluid. As expected, the  $\tau$  values in the Ebro River channel upstream of the confluence apex are very close to those predicted in the VR=0.08, Ri=0 simulation (Fig. 13). Downstream of the confluence apex, the main region of high  $\tau$  extends from the confluence apex to the South Bank and is induced by the near-bed current of denser fluid (Fig. 9b). The width of this region is about 30D, very close to the width of the near-bed current containing denser fluid from the Segre River. Relatively large  $\tau$  values are also recorded beneath the denser fluid current after it is deflected by the South Bank and moves parallel to it. The mean bed shear stress also increases beneath the region where the denser fluid from the Segre River accelerates and plunges down toward the bed to form the near-bed current. This region is situated near the Segre River bank line containing the confluence apex and also has a width of about 30D. Finally, relatively large  $\tau$  values are observed in the region where the less-dense fluid originating in the Ebro River that moved over the near-bed, cross-flow current from the Segre River penetrates again until the bed (Fig. 9b). This is expected because the higher streamwise velocity of the flow originating in the Ebro River tributary.

The first region where the amplification of  $\tau^{\text{rms}}$  is very significant is the one where the denser flow from the Segre River channel plunges toward the bed and interacts with the KH billows shed in the SSL forming at the confluence apex. Because of the mean recirculation bubble, strong interactions between the separated shear layer on the Ebro River side of the confluence apex and the attached boundary layer on the Segre River side occur (Fig. 5). These interactions lead to ejection of eddies from the attached boundary layer and result in a large amplification of the TKE and  $\tau^{\text{rms}}$  especially during the times when a new bubble forms near the confluence apex (e.g., see vorticity distribution at  $t=t_0+1000D/U_0$  in Fig. 5). The second region of high  $\tau^{\text{rms}}$  is the one where the near-bed current of denser fluid reaches the South Bank (Figs. 9b, 14b). Thus, bank erosion is expected to be of concern at the South Bank around section A. This was not the case in the  $VR=0.41$ ,  $Ri=0.67$  case [11], where no near-bed current of dense fluid formed. The other region where bank erosion may be of concern is at the Segre River bank line. It starts at the confluence apex and extends for about  $50D$  upstream into the Segre River channel. Finally, the lateral oscillations of the interface between the middle region containing less-dense fluid originating in the Ebro River tributary and the surrounding regions containing denser fluid induce an increase of  $\tau^{\text{rms}}$ .

Overall, the  $\tau$  and  $\tau^{\text{rms}}$  patterns in Figs. 13 and 14 show that erosion potential of the flow is larger in the  $Ri=0$  case especially on the Ebro River side of the main channel. Moreover,

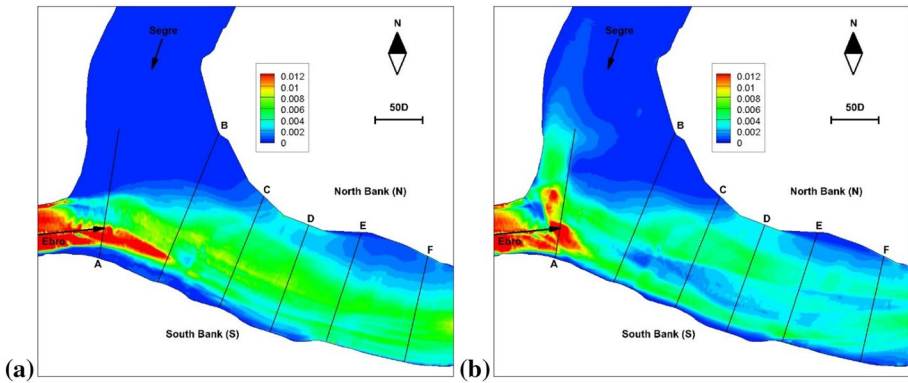


Fig. 13 Distribution of the bed shear stress magnitude,  $\tau/\rho U_0^2$ , in the mean flow. **a**  $Ri=0$ ; **b**  $Ri=1.89$

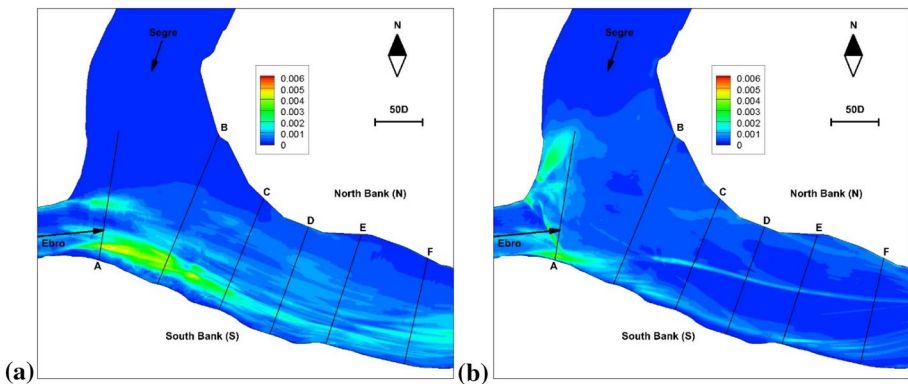


Fig. 14 Distribution of the rms of the bed shear stress magnitude,  $\tau^{\text{rms}}/\rho U_0^2$ . **a**  $Ri=0$ ; **b**  $Ri=1.87$



if the incoming flows carry fine suspended sediment, the formation of a sediment deposition bar in the  $Ri = 1.89$  case is possible downstream of section B. The bar is expected to develop in between the region of high  $\tau$  values induced by the interaction of the denser fluid with the South Bank and that forming beneath the high-speed fluid from the Ebro River (Fig. 13b). The only region where erosion is expected to be stronger in the  $Ri = 1.89$  case compared to the  $Ri = 0$  case is situated near the left bank line of the Segre River channel, in the vicinity of the confluence apex where the denser fluid is plunging toward the bed.

## 9 Final discussion and conclusions

Despite the smaller temperature difference between the two streams in the  $Ri = 1.89$ ,  $VR = 0.08$  simulation, stratification effects were larger compared to those observed in the  $VR = 0.41$  simulation discussed in Cheng and Constantinescu [11]. The higher value of the Richardson number was only partially responsible for the stronger stratification effects and mixing between the two streams observed in the  $Ri = 1.89$ ,  $VR = 0.08$  simulation. The other major contributor was that the Segre River tributary contained the denser fluid in the  $VR = 0.08$  simulation while it contained the less dense fluid in the  $VR = 0.41$  simulation. As a result, the intrusion of heavier fluid near the bed and of lighter fluid near the free surface developed in opposite directions in these two cases. This resulted in different mean flow patterns and major differences in the dynamics of the large-scale eddies generated inside the upstream part of the confluence hydrodynamic zone in the  $VR = 0.41$  and  $VR = 0.08$  cases with  $Ri \gg 0$ . Another important observation is that the discharge ratio in the  $VR = 0.08$ ,  $Ri = 1.89$  case was about 0.04, which means that the flow conditions in this case are close to those when a river is in contact with a reservoir containing denser fluid. For such conditions, buoyancy effects (e.g., lateral near-bed intrusion of heavier fluid into the main tributary) play a major role in the interaction between the two streams starting at the confluence apex. This is very different compared to most of the cases analyzed in the literature where stratification effects on the flow structure and mixing driven by stratification become important only in the downstream part of the confluence hydrodynamic zone.

Despite the development of lateral intrusions of denser fluid near the bed and of less-dense fluid near the free surface (e.g., of a spatially developing lock-exchange-like flow away from the confluence apex), the basic (free-surface) mixing pattern predicted in the  $VR = 0.41$ ,  $Ri = 0.67$  simulation was the one commonly observed at most confluences. The flow from each tributary remained on the same side of the main channel and most of the mixing took place at the interface separating the two regions. The same mixing pattern was observed in the no-density-effects ( $Ri = 0$ ) cases where, not surprisingly, no lateral intrusions of fluid from one region into the other one were observed along the mixing interface. By contrast, the free-surface mixing pattern was very different in the  $VR = 0.08$ ,  $Ri = 1.89$  simulation where three regions were present starting some distance from the confluence apex. Part of the incoming denser fluid from the Segre River remained on the same side of the main channel and moved parallel to the North Bank. Next to it, a region containing the less-dense fluid from the Ebro River was present. A region containing fluid with a density that was larger than that of the Ebro River was present near the South Bank. Such a flow distribution is impossible to occur in the absence of strong stratification effects that can generate a two-layer flow close to the confluence apex, where the denser flow in the lower layer and the less-dense flow in the top layer are moving in different directions. Near the free surface, the flow from the Segre River moved toward the bank containing the

confluence apex and then plunged down to form the near-bed current of denser fluid. This current moved across the main channel to reach the South Bank. From there it emerged back to the free surface and continued as a current moving in the vicinity of the South Bank, thus explaining the formation of the third region.

It is also relevant to mention that for large density differences between the flows in the main river and its tributary, the denser flow can plunge rapidly such that no visible mixing is observed near the free surface and the main channel contains only less dense fluid at the free surface. Such a case was documented at the confluence of the Rio Uruguay and one of its tributaries in Argentina where the denser stream carries lots of sediment including iron-rich earth [2]. The only possibility is that the denser fluid plunges toward the bed and most of the mixing with the surrounding less-dense fluid occurs below the free surface. Another relevant example is the concordant bed confluence between the Negro River and the Solimoes River which is characterized by different temperatures and sediment loads in the two tributaries. Though at most times the temperature difference is only 1–2 °C [26], sometimes the temperature of Rio Solimoes can be about 6 °C lower than that of the Rio Negro [3]. Furthermore, Rio Solimoes carries lots of sediment, which further acts toward increasing the density difference between the two streams. When such conditions occur, near the free surface, the less dense fluid from the Rio Negro is surrounded on its both sides by denser fluid originating in the Rio Solimoes for some distance downstream of the confluence apex. Such a flow pattern is impossible to be observed in the absence of strong density-difference effects and is consistent with the patterns observed near the free surface in the  $VR=0.08$ ,  $Ri=1.89$  simulation.

The large degree of bed discordance, the large difference of the bed elevations on the North Bank and South Bank sides of the main channel and the large-width of the small-discharge tributary resulted in a strong increase of the flow three-dimensionality especially close to the confluence apex. Meanwhile, no SOV cells formed in the region where the two streams collided. This was true for both the  $Ri=0$  and  $Ri=1.89$   $VR=0.08$  simulations, but 3-D effects were stronger in the  $Ri=1.89$  simulation. For example, in both cases large recirculating flow eddies formed near the confluence apex via the merging of KH vortices shed inside the SSL forming on the Ebro River side of the confluence apex. The formation and shedding of these eddies was close to periodic, though the period was more than one order of magnitude larger in the  $Ri=1.89$  simulation. In both cases, the vertical transport inside the cores of these eddies was significant. However, in the  $Ri=1.89$  simulation, these eddies were much larger and penetrated until the North Bank, where they started dissipating via interaction with the bank line. Their capacity to mix fluid as they moved away from the confluence apex was significant. The formation of the near-bed current of denser fluid and the mixing taking place at the interface with the fluid originating in the Ebro River provided another mixing mechanism not present in the  $Ri=0$  simulation.

Simulations conducted with  $VR=0.08$  and with the denser fluid in the low-discharge, shallower tributary showed that density contrast acted toward sharply increasing mixing between the two streams. The volume of well-mixed fluid was about 4 times larger in the  $Ri=1.89$  simulation compared to the  $Ri=0$  simulation at about 350D from the confluence apex. An increase of mixing with increased density difference between the incoming streams was also observed by Lane et al. [25], though in their case the denser fluid was in the deeper tributary. In contrast to this result, the streamwise variation of the amount of well-mixed fluid was fairly close in the  $Ri=0$  and  $Ri=0.67$  simulations with  $VR=0.41$ . This shows that stratification induced by density differences between the incoming streams may induce faster mixing but that the end effect is a function of several other flow and

geometrical parameters including density ratio between the faster and the slower tributary, planform geometry, degree of bed discordance, bathymetry and velocity ratio.

The finding that stratification induced by density differences in the incoming streams can act toward strongly enhancing the overall mixing between the incoming flows is consistent with the findings of Ramón et al. [38] for the same confluence. It contradicts the standard assumption that stratification always acts toward weakening mixing because of the damping effect on the KH billows generated in mixing layers under stratified flow conditions. Moreover, the classical model of two streams flowing side by side while mixing does not apply for such cases.

Future work is needed to clarify the effect of increasing density contrast between the two tributaries on hydrodynamics and mixing at confluences with varying degree of bed discordance. This requires conducting a comprehensive parametric study for idealized-geometry confluences. The present study assumed that the secondary flow is negligible in the incoming tributaries. This is not the case if the confluence apex is situated close to regions of high channel curvature in one or both tributaries. Provided field data are available, the present model can be used to investigate the effects of secondary flow in the oncoming tributary. This work considered density differences due to only temperature differences between the incoming flows. In many river confluences density contrast is due to differences in both the temperature and the sediment load of the two tributaries. Stratification effects are not expected to be the same if the same density difference between the two streams is due only to differences in the temperature, only to differences in the sediment load or to a combination of differences in the temperature and sediment load. Such effects can be simulated by adding a transport equation for the suspended sediment and/or a bed load model.

**Acknowledgements** The authors would like to thank Dr. J. Prats-Rodriguez, Prof. E. Blade and Prof. J. Dolz for providing the bathymetry data and flow conditions needed to perform the simulations, as well as for insightful discussions. The authors would like to thank Dr. Anand Padmanabhan and the National Center for Supercomputing Applications (NCSA) at the University of Illinois at Urbana-Champaign (UIUC) for providing the computational resources needed to perform the simulations. This work was supported by the BCS Geography and Spatial Sciences Program of the US National Science Foundation under GRANT No. 1359836. Any opinions, findings, and conclusions or recommendations expressed in this material are those of the authors and do not necessarily reflect the views of the U.S. National Science Foundation.

## References

1. Arbat-Bofill M, Palau A, Sanchez-Junni M, Castellet EB, Ninerola D, Dolz J (2014) Hydrodynamics of Ribarroja Reservoir (Ebro River, Spain): water temperature, water velocities and water age. In: Schleiss A (ed) Proceedings of the RiverFlow 2014 international conference on fluvial hydraulics, Lausanne, Switzerland. Taylor and Francis, London
2. Arthus-Bertrand Y, Burleigh R (2005) Earth from above. Publisher Harry Abrams, New York. ISBN 081095947X
3. Beluco A, de Souza PK (2014) Energy at the junction of the Rivers Negro and Solimoes, contributors of the Amazon River, in the Brazilian Amazon. Int Sch Res Notices 2014, 794583. <https://doi.org/10.1155/2014/794583>
4. Best J, Parsons D, Kellman P, Amsler M, Szupiany R, Kostaschuck R, Lane S, Hardy R, Orfeo O (2007) On the influence of density contrasts between mixing flows at channel confluences: the Río Bermejo and Río Paraguay, Argentina. Workshop on Morphodynamic Processes in Large Lowland Rivers, Santa Fe, Argentina, November 2007
5. Best JL, Rhoads B (2008) Sediment transport, bed morphology and the sedimentology of river channel confluences. In: Rice S, Roy A, Rhoads B (eds) River confluences, tributaries and the fluvial network. Wiley, Hoboken, pp 45–72. <https://doi.org/10.1002/9780470760383.ch4>

6. Boyer C, Roy AG, Nest JL (2006) Dynamics of a river channel confluence with discordant beds: flow turbulence, bed load sediment transport, and bed morphology. *J Geophys Res* 111:F04007
7. Bouchez J, Lajeunesse E, Gaillardet J, France Lanord C, Dutra Maia P, Maurice L (2010) Turbulent mixing in the Amazon River: the isotopic memory of confluences. *Earth Planet. Sci Lett* 290:37–43
8. Bradbrook KF, Lane SN, Richards KS (1998) Investigation of controls on secondary circulation in a simple confluence geometry using a three-dimensional model. *Hydrol Process* 12:1371–1396
9. Chang KS, Constantinescu G, Park SO (2007) Assessment of predictive capabilities of Detached Eddy Simulation to simulate flow and mass transport past open cavities. *ASME J Fluids Eng* 129(11):1372–1383
10. Cheng Z, Constantinescu G (2014) Spatial development of constant-depth shallow mixing layer in a long channel. In: International conference on fluvial hydraulics, River Flow 2014, Lausanne, Switzerland
11. Cheng Z, Constantinescu G (2018) Stratification effects on flow hydrodynamics and mixing at a confluence with a highly discordant bed and a relatively low velocity ratio. *Water Resour Res* 54(7):4537–4562. <https://doi.org/10.1029/2017WR022292>
12. Cheng Z, Koken M, Constantinescu G (2018) Approximate methodology to account for effects of coherent structures on sediment entrainment in RANS simulations with a movable bed and applications to pier scour. *Adv Water Resour.* <https://doi.org/10.1016/j.advwatres.2017.05.019>
13. Constantinescu G (2014) LE of shallow mixing interfaces: a review. *Environ Fluid Mech* 14:971–996. <https://doi.org/10.1007/s10652-013-9303-6>
14. Constantinescu G, Chapelet MC, Squires KD (2003) Turbulence modeling applied to flow over a sphere. *AIAA J* 41(9):1733–1743
15. Constantinescu G, Miyawaki S, Rhoads B, Sukhodolov A, Kirkil G (2011) Structure of turbulent flow at a river confluence with a momentum and velocity ratios close to 1: insight from an eddy-resolving numerical simulation. *Water Resour Res* 47:W05507. <https://doi.org/10.1029/2010WR010018>
16. Constantinescu G, Miyawaki S, Rhoads B, Sukhodolov A (2012) Numerical analysis of the effect of momentum ratio on the dynamics and sediment entrainment capacity of coherent flow structures at a stream confluence. *J Geophys Res Earth Surface* 117:F04028. <https://doi.org/10.1029/2012JF002452>
17. Constantinescu G, Miyawaki S, Rhoads B, Sukhodolov A (2014) Numerical evaluation of the effects of planform geometry and inflow conditions on flow, turbulence structure, and bed shear velocity at a stream confluence with a concordant bed. *J Geophys Res Earth Surface* 119:2079–2097. <https://doi.org/10.1002/2014JF003244>
18. Constantinescu G, Miyawaki S, Rhoads B, Sukhodolov A (2016) Influence of planform geometry and momentum ratio on thermal mixing at a stream confluence with a concordant bed. *Environ Fluid Mech* 16(4):845–873. <https://doi.org/10.1007/s10652-016-9457-0>
19. De Serres B, Roy AG, Best JL (1999) Three-dimensional structure of flow at a confluence of river channels with discordant beds. *Geomorphology* 26:313–335
20. Gaudet JM, Roy AG (1995) Effect of bed morphology on flow mixing length at river confluences. *Nature* 373:138–139
21. Guillén-Ludeña S, Franca MJ, Cardoso AH, Schleiss AJ (2015) Hydro-morphodynamic evolution in a 90 movable bed discordant confluence with low discharge ratio. *Earth Surf Proc Land* 40(14):1927–1938. <https://doi.org/10.1002/esp.3770>
22. Guillén-Ludeña S, Franca MJ, Cardoso AH, Schleiss AJ (2016) Evolution of the hydromorphodynamics of mountain river confluences for varying discharge ratios and junction angles. *Geomorphology* 255:1–15. <https://doi.org/10.1016/j.geomorph.2015.12.006>
23. Guillén-Ludeña S, Cheng Z, Constantinescu G, Franca MJ (2017) Hydrodynamics of mountain river confluences and its relationship to sediment transport. *J Geophys Res Earth Surface* 122:901–924. <https://doi.org/10.1002/2016JF0044122>
24. Konsoer K, Rhoads B (2014) Spatial–temporal structure of mixing interface turbulence at two large river confluences. *Environ Fluid Mech* 14(5):1043–1070
25. Lane SN, Parsons DR, Nest JL, Orfeo O, Kostaschuk RA, Hardy RJ (2008) Causes of rapid mixing at a junction of two large rivers: Rio Parana and Rio Paraguay, Argentina. *J Geophys Res* 113:F02019. <https://doi.org/10.1029/2006JF000745>
26. Laraque A, Guyot JL, Filizola N (2009) Mixing processes in the Amazon River at the confluences of the Negro and Solimões rivers, Encontro das Águas, Manaus, Brasil. *Hydrol Process* 23:3131–3140
27. Leite Ribeiro M, Blanckaert K, Roy AG, Schleiss AJ (2012) Flow and sediment dynamics in channel confluences. *J Geophys Res* 117:F01035. <https://doi.org/10.1029/2011JF002171>

28. Leite Ribeiro M, Blanckaert K, Roy AG, Schleiss AJ (2012) Hydromorphological implications of local tributary widening for river rehabilitation. *Water Resour Res* 48(10):10528
29. Leite Ribeiro M, Blanckaert K, Schleiss AJ (2014) Local tributary widening for river rehabilitation. *Ecohydrology* 9(2):204. <https://doi.org/10.1002/eco.1588>
30. Lewis QW, Rhoads B (2015) Rates and patterns of thermal mixing at a small stream confluence under variable incoming flow conditions. *Hydrol Process* 29:4442–4456. <https://doi.org/10.1002/hyp10496>
31. Lyubimova T, Lepikhin A, Konovalov V, Parshakova Y, Tiunov A (2014) Formation of the density currents in the zone of confluence of two rivers. *J Hydrol* 508:328–342
32. Martí-Cardona B, Arbat-Bofill M, Prats J, Pipia L (2016) Thermal remote sensing for reservoir modelling and management. *Living planet symposium*, May 2016, Prague, Czech Republic. SP-740
33. Orr TS, Domaradzki JA, Spedding GR, Constantinescu G (2015) Description of the near wake of a sphere in a steady horizontal motion through a linearly stratified fluid at  $Re = 10000$ . *Phys Fluids* 27:035113. <https://doi.org/10.1063/1.4915139>
34. Paola C (1997) When streams collide. *Nature* 387:232–233
35. Prats J, Armengol J, Marcé R, Sánchez-Juny M, Dolz J (2010) Dams and reservoirs in the lower Ebro River and its effects on the river thermal cycle. *Hdb Environ Chem* 13:77–95
36. Ramón CL, Hoyer AB, Armengol J, Dolz J (2013) Mixing and circulation at the confluence of two rivers entering a meandering reservoir. *Water Resour Res* 49:1429–1445
37. Ramón CL, Prats J, Rueda F (2016) The influence of flow inertia, buoyancy, wind, and flow unsteadiness on mixing at the asymmetrical confluence of two large rivers. *J Hydrol* 539:11–26
38. Ramón CL, Armengol J, Dolz J, Prats J, Rueda F (2014) Mixing dynamics at the confluence of two large rivers undergoing weak density variations. *J Geophys Res-Oceans* 119(4):2386–2402
39. Rice SP, Kiffney P, Greene C, Pess GR (2008) The ecological importance of tributaries and confluences. In: Rice SP, Roy AG, Rhoads BL (eds) *River confluences, tributaries and the fluvial network*. Wiley, Chichester, pp 209–242
40. Riley JD, Rhoads B, Parsons DR, Johnson KK (2015) Influence of junction angle on three-dimensional flow structure and bed morphology at confluent meander bends during different hydrological conditions. *Earth Surf Proc Land* 40:252–271
41. Rodi W, Constantinescu G, Stoesser T (2013) *Large eddy simulation in hydraulics* IAHR monograph. CRC Press, Boca Raton. ISBN-10-1138000247
42. Roy AG, Bergeron N (1990) Flow and particle paths in a natural river confluence with coarse bed material. *Geomorphology* 3:99–112
43. Roy AG, Roy R (1988) Changes in channel size at river confluences with coarse bed material. *Earth Surf Proc Land* 13:77–84
44. Roy AB, Roy R, Bergeron N (1988) Hydraulic geometry and changes in flow velocity at a river confluence with coarse bed material. *Earth Surf Proc Land* 13:583–598
45. Sukhodolov A, Krick J, Sukhodolova T, Cheng Z, Rhoads B, Constantinescu G (2017) Turbulent flow structure at a discordant river confluence: asymmetric jet dynamics with implications for channel morphology. *J. Geophys Res Earth Surface* 122:1278–1293. <https://doi.org/10.1002/2016JF004126>
46. Tang H, Zhang H, Yuan S (2017) Hydrodynamics and contaminant transport on a degraded bed at a 90-degree channel confluence. *Environ Fluid Mech* 18(2):443–463
47. Le Trung B, Khosronejad A, Sotiropoulos F, Bartelt N, Woldeamlak S, Dewall P (2019) Large-eddy simulation of the Mississippi River under base-flow condition: hydrodynamics of a natural diffuence-confluence region. *J Hydraul Res* 57(6):836–851
48. Yalin MS, da Silva AMF (2001) *Fluvial processes*. Kluwer (IAHR) Monograph, Delft. ISBN 90-805649-2-3
49. Yuan S, Tang H, Qiu X, Xia Y (2018) Water flow and sediment transport at open channel confluences: an experimental study. *J Hydraul Res* 56(3):335–350
50. Zeng J, Constantinescu G, Weber L (2010) 3D calculations of equilibrium conditions in loose-bed open channels with significant suspended sediment load. *J Hydraul Eng* 136(9):557–571. [https://doi.org/10.1061/\(ASCE\)HY.1943-7900.0000213](https://doi.org/10.1061/(ASCE)HY.1943-7900.0000213)
51. Zilitinkevich SS, Elperin T, Kleerorin N, Rogachevskii I (2007) Energy- and flux-budget (EFB) turbulence closure model for stably stratified flows. *Bound Layer Meteorol* 125:167–191

## Affiliations

Zhengyang Cheng<sup>1,2</sup> · George Constantinescu<sup>1</sup> 

<sup>1</sup> Department of Civil and Environmental Engineering and IIHR-Hydroscience and Engineering, The University of Iowa, Iowa City, IA 52242, USA

<sup>2</sup> Hydrologic Research Center, San Diego, CA 92127, USA